Sintering Plasma-Synthesized Silicon Germanium Nanocrystals

A THESIS

SUBMITTED TO THE FACULTY OF

UNIVERSITY OF MINNESOTA

BY

Ranee I. Skinner

IN PARTIAL FULFILLMENT OF THE REQUIREMENTS

FOR THE DEGREE OF

MASTER OF SCIENCE

Prof. Uwe R. Kortshagen, Adviser

May 2016

ACKNOWLEDGEMENTS

My deepest gratitude is extended to everyone who made this work possible and saw me through graduate school. First, a googol of thanks go to Gjeni and Zach for putting up with me through my career change over the last three years. You are the best family I could possibly ask for, and I could not have accomplished this without your support.

Special thanks also go to my adviser, Professor Kortshagen, for taking a chance on a political scientist with a year of physics background. You have changed my life more than you know. I am eternally grateful for your guidance and encouragement the past two years.

I owe a great debt to my fellow researchers in the Kortshagen Group who took the time to train me, troubleshoot problems with me, and brainstorm ideas. In particular, I would like to thank Nic Kramer, Katelyn Schramke, and Katharine Hunter for all the time they spent with me and Claudia Gorynski for proving to be a brilliant partner in IPL experiments. Amanda Dillman from the Kohlstedt Rock and Mineral Physics Lab provided many hours of assistance in hot pressing pellets, and Jacob Held did remarkable microscopy on the resulting samples. Thank you all, and all of the unmentioned collaborators, for there are too many to list.

Thank you to my family (Scott, Sue, Ryan, and Rich) and my campaign family (Cristine, Justin, Peter, Michael, and Sam) for feeding me, making me laugh, and giving countless pep talks. Thank you to Cristine for always lobbying for me. Thank you to my grandma Judy for making me as stubbornly persistent as her and believing in me even when I don't. Thank you to Heather for listening to me talk about nothing but my research for months on end.

Finally, thank you to the late Kent Berg for profoundly changing my life in the short time we knew each other and inspiring me to change careers. I am much happier as an engineer.

Dedicated in fondest memory of Kent Berg. Thank you for inspiring this journey.

ABSTRACT

Alloyed silicon germanium is a group IV semiconductor that has been used for its thermoelectric properties for over 40 years. The thermoelectric figure of merit is proportional to a material's electrical conductivity and Seebeck coefficient squared, while it is inversely proportional to the thermal conductivity. It has repeatedly been shown that the dimensionless thermoelectric figure of merit can be increased by nanostructuring silicon germanium to reduce the lattice thermal conductivity of the material. Plasma synthesized silicon germanium nanocrystals offer the potential to meet this need with the added benefit of being able to fine tune the material's properties by adding dopants, altering the silicon germanium ratio, and changing the nanoparticle size.

Silicon germanium nanocrystals were synthesized in intrinsic, boron-doped, and phosphorous-doped film and powder form in a capacitively coupled radio frequency plasma. They were characterized extensively to determine composition and verify crystallinity. Due to the nanostructured alloy form, the thermal conductivity will easily meet the needs for a high thermoelectric figure of merit. Films and powders as synthesized are extremely electrically insulating. In order to increase electrical conductivity to make the material useful, several post-treatment processes were investigated to sinter the nanoparticles. Rapid thermal annealing, hot pressing, laser sintering, and intense pulsed light sintering were attempted. The results of these efforts are presented in this thesis along with ideas for future investigation.

TABLE OF CONTENTS

LIST OF TABLES

LIST OF FIGURES

CHAPTER 1: INTRODUCTION

1.1 SILICON GERMANIUM

Somewhere just beyond our solar system, the Voyager 1 spacecraft, launched in 1977, glides through darkness exploring the furthest of humanity's reaches. The 39-year-old craft faithfully sends back scientific data as it plods along through interstellar space. With our sun showing as only a bright dot in the black expanse behind it, the common solar panels powering today's spacecraft would be useless. After 39 years, any stored battery energy would be gone. Instead, Voyager 1 sports three Radioisotope Thermoelectric Generators (RTG's).[1] Plutonium centers provide a heat source for the RTG's, and silicon germanium unicouples turn that heat into electricity to power the spacecraft.

Separately, silicon and germanium are widely-used group IV semiconductors. Silicon is one of the most abundant materials on Earth.[2] Inexpensive due to its abundance, silicon is the most commonly used semiconductor in the production of electronics. Sitting right below silicon on the periodic table is germanium. Germanium is less abundant and about a hundred times as expensive as silicon, resulting in it being used far less in semiconductor technologies.

Alloyed together, silicon germanium (SiGe or $Si_{1-x}Ge_x$ in specific compositions) has a unique ability – it is a good thermoelectric material that produces a usable voltage over a temperature gradient.[3] In the case of the Voyager spacecraft, this temperature gradient is provided by the heat of decaying radioactive material on one side of the SiGe and the cold emptiness of space on the other. Silicon germanium is commonly used for thermoelectric applications due its relatively low cost and low toxicity compared to other candidate materials.[3] Outside of thermoelectrics, silicon germanium is often used in manufacturing transistors. It offers higher forward and lower reverse gain than silicon-only transistors which translates to better performance.[4] By changing the germanium fraction, fundamental material properties like the band gap can be finely tuned for a specific application. [3,5]

1.2 THERMOELECTRICS

For 39 years, Voyager 1 has been functioning without so much as a tune-up. The RTG technologies powering Voyager and other thermoelectric devices boast long lifespans, require no or low maintenance, and have no moving parts. They provide a clean conversion of thermal to electrical energy and do not emit greenhouse gases. Aside from their extraterrestrial applications, they can be used in conjunction with renewable energy technologies such as solar concentrators and photovoltaics[6], as miniaturized thermoelectric generators in microelectronic circuitry,[7] or used in solid state refrigeration devices[8,9]. The efficiency of thermoelectric materials is presently low, preventing wider use of them.

When one side of a material is heated, free carriers within it will diffuse toward the cold side. As charge builds at one side of the material, an electrical potential arises. This is called the Seebeck effect. The Seebeck coefficient, or thermopower, quantifies this effect as the change in voltage produced from the hot to cold sides of the material over a change in temperature. It is expressed in units of V/K and written as,

$$S = -\frac{\Delta V}{\Delta T}$$

where the negative sign is a convention that results in semiconductors with electrons as the majority carrier (n-type) having a negative Seebeck and those with holes as the majority carrier (p-type) having a positive Seebeck coefficient. It is noteworthy here that a large Seebeck coefficient necessitates a high carrier concentration of a single type of charge carrier. However, doping concentrations of greater than 10^{20} cm^{-3} become unfavorable.[10]

While all conducting materials exhibit the Seebeck effect, there are more requirements for thermoelectric applications. Thermoelectric materials are evaluated based on their efficiency with the dimensionless thermoelectric figure of merit ZT[3,11],

$$ZT = \frac{S^2\sigma}{\kappa}T$$

with an electrical conductivity σ, and thermal conductivity κ for a temperature T. $S^2\sigma$ is often referred to as the power factor.[12] Semiconductors have higher power factors than metals or insulators, making them optimal for thermoelectric applications.[13] The thermal conductivity of the material can be broken into two major components, the lattice thermal conductivity κ_l and electronic thermal conductivity κ_e where,

$$\kappa = \kappa_l + \kappa_e \ .$$

At very high temperatures, a third contribution from the bipolar effect is added to the thermal conductivity. At temperatures under 1000K, the lattice thermal conductivity in $Si_{0.8}Ge_{0.2}$ is triple that of the electronic, and the bipolar contribution is negligible.[10]

For a thermoelectric material to have a high efficiency, it must have a high Seebeck coefficient, high electrical conductivity, and low thermal conductivity. The ideal material has been described as having phonon-glass, electron-crystal properties, since phonons should be impeded as in a glass and electrons free as in a crystal.[12] The parameters, however, are not independent of each other.[14] For instance, the electronic contribution to the thermal conductivity is directly proportional to the electrical conductivity of a material.[15] Any benefit from reducing κ_e will then be offset by the decrease in σ. Similarly, increasing carrier concentration in a material can increase the electrical conductivity, σ, but reduce the Seebeck coefficient, S, by rapidly increasing the Fermi energy.[15]

Alloys, like silicon germanium, have favorable thermoelectric properties because of a reduced thermal conductivity. In both crystalline silicon and germanium, atoms form a periodic diamond crystal lattice.[16] Phonons, vibrations propagating through the lattice, make up the lattice thermal conductivity. Very short mean free path phonons are able to propagate through the lattice due to the periodicity of the pure materials. In alloyed SiGe, the small Si atoms and larger Ge atoms form a lattice together. Over 50 years ago, this mismatch in atomic sizes was discovered to cause the shorter mean free path phonons to scatter and decrease lattice thermal conductivity, κ_l. This discovery formed the basis for SiGe thermoelectric devices still used today.[17,18]

Most approaches to increasing ZT in the last 20 years have risen from the idea of further reducing the lattice thermal conductivity through nanostructuring.[19–24] Models predict that a large portion of phonons in $Si_{0.8}Ge_{0.2}$ have a mean free path of over 100 nm.[22] If the material is nanostructured to have smaller grains than this, longer mean free path (lower frequency) phonons are scattered such that the phonon mean free path is constricted to the size of the grain, significantly reducing the lattice thermal conductivity.

Undoped bulk silicon germanium is not an optimal thermoelectric material due to its low electrical conductivity. As in any semiconductor, impurities can be added to silicon germanium to add extra electrons or holes to the lattice, which increase the electrical conductivity. By doping the material, ZT values of around 0.65 for bulk p-type[17,25] and 0.93 for n-type[20] can be achieved at 900°C. Increases to 0.95 in p-type[21] and 1.3 in n-type[20] have been reported through nanostructuring silicon germanium with a ball milling approach. While having produced high efficiency values, the ball milling approach has some drawbacks. It requires a large amount of energy to crush bulk materials, it often produces large and irregular-shaped particles, and dopant incorporation into the lattice can be difficult.[10]

Plasma-synthesized nanocrystals (NCs) have advantages over conventional SiGe NC synthesis processes like ball milling. A capacitively-coupled, radio-frequency plasma can produce highly crystalline and monodisperse nanoparticles of uniform composition in high yield.[26,27] Alloys such as SiGe can be produced with easily tunable compositions, are easily doped to p- or n-type, and are size tunable in the 5-20nm range.[28,29] This thesis investigates the possible use of plasma-synthesized silicon germanium nanocrystals in thin film and thermoelectric applications. It focuses on possible sintering methods to improve the density and conductivity of NC powders and films and offers insight into future avenues of research.

CHAPTER 2: SYNTHESIZING SIGE NANOCRYSTALS

2.1 PLASMA REACTOR DESIGN

Silicon germanium nanoparticles were synthesized in a non-thermal, low-pressure, capacitively-coupled, radio-frequency (RF) plasma. Argon, 100% silane (SiH_4), and 10% germane (GeH_4) diluted in argon are used as precursor gases. Phosphine (PH_3) and diborane (B_2H_6) can be flowed with the silane and germane mixture to dope the particles with phosphorus (n-type) or boron (p-type).

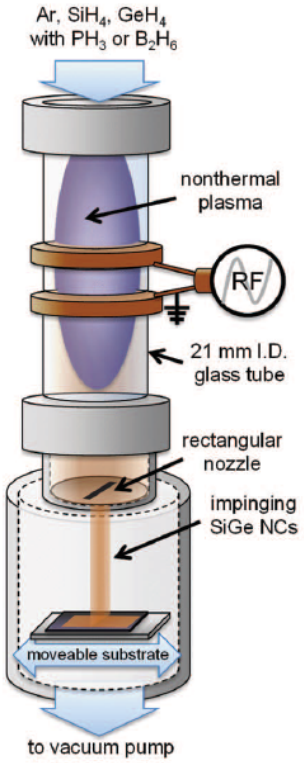

Figure 1: Plasma reactor schematic. A capacitively-coupled, radio frequency plasma is used for nanoparticle synthesis.[29]

Figure 1 shows the reactor design, with precursor gases entering the top of the reactor.[29] The gases move through a 1-inch outer diameter glass tube encompassed by a

circular RF-driven electrode and a second grounded electrode below it. The plasma is driven at 13.56 MHz with an Advanced Energy RFX 600 RF Power Supply. A MFJ Enterprises Versa Tuner is used to match the impedance of the plasma, a necessary step to provide enough energy to dissociate precursor gases for nanoparticle formation.[30] The power supply is capable of supplying 600 W, however, the matching network overheats when used above 130 W. The powers listed here are nominal values. The actual power supplied to the plasma is likely much lower, since experience proves that other configurations of electronics will produce similarly crystalline nanoparticles at vastly different powers.

In the region where the plasma is ignited, the gas pressure of argon and other precursors is 1 Torr or less, as measured by a Pirani gauge. Before flowing precursor gases, the reactor is purged with nitrogen three times to remove contaminants and brought to base pressure with an Alcatel 2033/63 vacuum pump. Base pressures usually hover around 9 mTorr with a leak rate of 10 mTorr/min or less. An argon cleaning plasma is run for 5 minutes before adding silane, germane, and dopants to remove any other contamination, such as solvents, from the glass tube. An argon flow is established as a carrier gas in the plasma. Precursor gas flows are added and metered by MKS Instruments 1179 and 1479 mass flow controllers (MFCs) dedicated to each gas.

An adjustable rectangular slit nozzle sits below the plasma, restricting the flow of the gas and nanoparticle mixture. The nozzle serves to regulate pressure and the residence time of the precursor gases, which controls nanoparticle growth. It also accelerates the particles to impact them on a substrate below the nozzle. The substrate is on a rod aligned to sit about 14 mm below the nozzle. The nanoparticles quickly lose velocity after exiting the nozzle, making the standoff distance of the substrate very important.[31]

An enclosed load-lock that connects to the reactor allows the substrate to be moved forward and back with a steel rod to raster a thin film stream of particles on the substrate. It forms a rectangular shape with a width of 12-14 mm, depending on the substrate standoff distance, and a length up to 10 cm. After synthesis, the sample is pulled back into the load-lock and filled with nitrogen to atmospheric pressure until the samples can be transferred to a

nitrogen-purged glovebox. Samples are stored in the glove box until characterization or post-synthesis treatment to prevent oxidization of the nanoparticles.

2.2 SILICON GERMANIUM NANOCRYSTAL SYNTHESIS

Alloyed silicon germanium particles were synthesized using a base recipe listed in Table 1 to produce $Si_{0.75\text{-}0.8}Ge_{0.25\text{-}0.2}$, which is identified in the literature as the optimal composition for thermoelectric applications.[18] The particles were deposited on either microscope slide glass, fused quartz, aluminum coated silicon wafer, thermal oxide silicon wafer, or pieces of a B-doped silicon wafer depending on the post-synthesis treatment and characterization to be performed. When collecting powders for bulk processes, a glass slide was used to impact piles of the nanopowder at a deposition rate of about 1 mg per minute. The NCs were characterized using X-Ray Diffraction (XRD), Fourier Transform Infrared Spectroscopy (FTIR), Raman spectroscopy, Secondary Electron Microscopy (SEM), and Scanning Transmission Electron Microscopy (STEM).

Table 1: Synthesis conditions for silicon germanium nanocrystals. All recipes used a nozzle size of 12mm by 0.61mm and a one-inch diameter tube. The plasma was driven at 13.56 MHz, 110W.

NC Type	SiH_4 (100%)	GeH_4 (10% in Ar)	PH_3 (15% in H_2)	B_2H_6 (10% in H_2)	Argon	Pressure (mTorr)
$Si_{.75\text{-}.8}Ge_{.25\text{-}.2}$	0.82 sccm	2.5-2.7 sccm	0	0	30 sccm	675-710
N-type $Si_{.75\text{-}.8}Ge_{.25\text{-}.2}$	0.82 sccm	2.5-2.7 sccm	0.38 sccm	0	30 sccm	690-730
P-type $Si_{.75\text{-}.8}Ge_{.25\text{-}.2}$	0.82 sccm	2.5-2.7 sccm	0	0.28 sccm	30 sccm	685-720

2.3 X-RAY DIFFRACTION CHARACTERIZATION

Nanoparticles targeted to be $Si_{0.8}Ge_{0.2}$ were synthesized using the base recipe in Table 1 with a germane flow of 2.6 standard cubic centimeters per minute (sccm). The target NC silicon germanium ratio takes into consideration the lower incorporation of germanium than

silicon reported by other researchers.[28,29] The crystallinity, size, and composition of the nanoparticles were probed with an X-ray Diffractometer (XRD). In a crystalline material, atoms coherently diffract light, creating a pattern that reveals information about the crystal in XRD.[32] In crystalline silicon and germanium, atoms organize into diamond cubic lattices, as do alloys of them.[16] The interplanar spacing, *d*, for the diamond cubic crystal lattice is described in terms of the Miller indices, *h k l*, and the lattice constant, a.[33]

$$d_{h,k,l} = \frac{a}{\sqrt{h^2 + k^2 + l^2}}$$

The lattice constant for silicon is 5.431 Å, and the lattice constant for germanium is 5.658 Å.[34] Respectively, this makes the interplanar spacing of the (111) plane of these materials 3.136 Å and 3.267 Å.

Data was collected on a Bruker D8 Discover X-Ray Diffractometer with a cobalt Kα source and VÅNTEC-500 area detector, and the signal was converted to a copper source of wavelength (λ) 1.54059 Å, which is more common in the literature, using Jade software (Materials Data Incorporated). With the interplanar spacing, the position of the (111) peak can be predicted using Bragg's Law[32,33],

$$2d \sin\theta = n\lambda \, .$$

The (111) plane diffraction will center around a two-theta position of 28.44° for silicon and 27.28° for germanium. When silicon and germanium are alloyed, the diamond cubic lattice parameter will change proportionally to the ratio of silicon to germanium and a single diffraction peak will be seen in between where the silicon and germanium peaks would be found in a non-alloyed mixture. Using Vegard's Law, the peak position can be used to closely approximate the silicon to germanium ratio of the nanocrystals.[34] This information is summarized in Table 2. A very small deviation from these predicted lattice parameters is found, however, it is generally less than one tenth of one percent.[5]

Table 2: X-ray diffraction values for silicon, germanium, and a silicon germanium alloy.

Composition	Lattice constant (Å)	d_{111} (Å)	Two-theta (Cu XRD)
Si	5.431	3.136	28.44°
$Si_{0.8}Ge_{0.2}$	5.476	3.162	28.21°
Ge	5.658	3.267	27.28°

Figure 2a shows XRD spectra of the (111)-plane peak for synthesized Si, Ge, $Si_{0.75}Ge_{0.25}$, and a mix of Si and Ge particles. In the alloyed particles, a single SiGe peak is visible, while two separate Si and Ge peaks are visible in the mixed sample.

The XRD spectra were fit with a peak analyzer using MDI Jade software. The full-width half maximum of a peak can be used to determine average nanocrystal size via the Scherrer equation. These fits were made within Jade using 7th order pseudo Voigt background fits for consistency. Jade software reports an "XS(Å)" (crystallite size) value for each of the (111)-, (200)-, and (311)-plane peaks, which were averaged and used as the diameter of the nanocrystal. High angle crystallite broadening, low angle peak asymmetry, specimen broadening, and choice of background fitting can all affect the accuracy of the size measurement,[35] therefore these values were taken to be good approximations and useful for relative size comparison, not as absolute values.

XRD shows a crystallite size of about 8 nanometers and a composition of $Si_{0.78}Ge_{0.22}$ for a gas flow ratio of 76% silicon and 24% germanium. This is consistent with the slightly lower incorporation of germanium than silicon reported by other researchers.[28,29] The clear peaks seen in the XRD spectra indicate a highly crystalline sample.

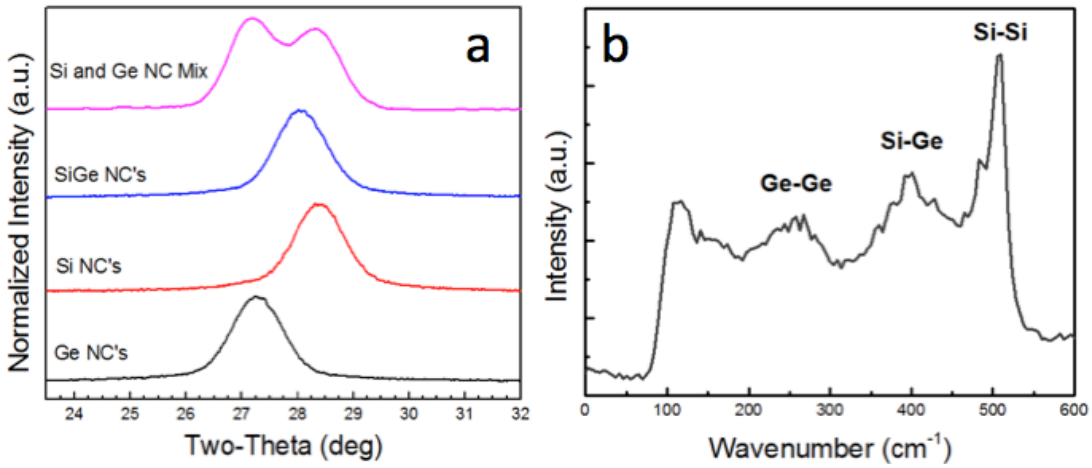

Figure 2: XRD and Raman Spectroscopy of SiGe. a) XRD spectra of Ge, Si, SiGe, and a mix of Si and Ge NCs show distinct peak positions for each material. Alloyed SiGe exhibits a single peak while mixed Si and Ge shows two. b) Raman spectroscopy shows crystalline SiGe, however, intense interference likely caused by Rayleigh scattering makes crystalline fraction difficult to determine.

2.4 RAMAN SPECTROSCOPY CHARACTERIZATION

Raman spectroscopy was employed to verify the crystallinity of the nanoparticles. A Witec Alpha300R confocal Raman microscope with a 532 nm laser wavelength source was used in conjunction with a DV401 CCD detector and UHTS300 spectrometer. Raman spectra taken of 8nm SiGe NCs (Figure 2b) shows clear peaks for the Si-Si, Ge-Ge, and Si-Ge bonds present in the alloy around 500, 275, and 400 cm^{-1}, respectively.[36] An additional peak can be seen here around 100 cm^{-1} which is likely signal contamination from intense Rayleigh scattering of the laser.[37] The Si-Si undergoes a shift to lower wavenumbers with increasing germanium ratio[16], making this data consistent with the target ratio of silicon to germanium. Raman spectroscopy is often used to determine amorphous to crystalline fraction, however, the signal interference could not be eliminated, making quantitative analysis difficult.

2.5 FOURIER TRANSFORM INFRARED SPECTROSCOPY CHARACTERIZATION

Boron and phosphorus doped SiGe were produced using the recipes listed in Table 1 and deposited in a thin film on silicon wafer coated with 300 nm of aluminum. They were transferred air-free to a nitrogen-purged glovebox where diffuse reflectance Fourier transform infrared spectroscopy (DRIFTS) measurements where performed using a Bruker Alpha IR spectrometer. Fourier transform infrared spectroscopy (FTIR) detects vibrations in atomic bonds, and the energy of these bonds is directly proportional to the wavenumber. FTIR allows characterization of surface chemistry of the nanoparticles, particularly showing the hydrogen termination of the NCs and oxidation of the samples.

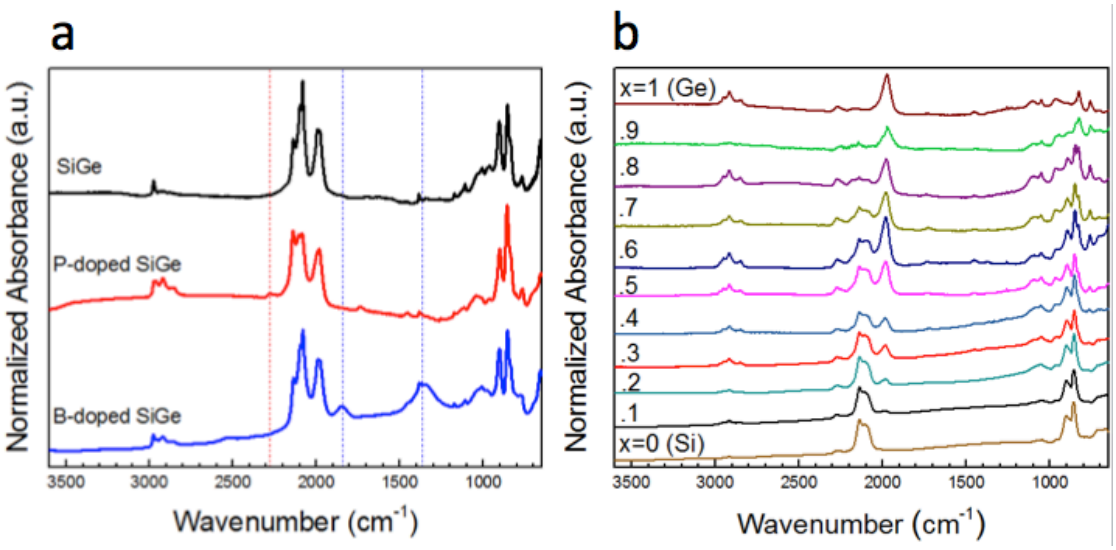

Figure 3: (a) FTIR of doped SiGe. FTIR absorbance of undoped, phosphorus-doped, and boron-doped $Si_{0.8}Ge_{0.2}$ exhibit the telltale dopant bonds in hydrogen-terminated NCs as well as a slight oxidation of the particles. The blue vertical dotted lines correspond to boron bond wavenumbers, while the red dotted line corresponds to phosphorous. (b) FTIR absorbance of 10% phosphorous-doped $Si_{1-x}Ge_x$ is shown in increments of x=.1. Phosphorous peaks are visible throughout the range of compositions, and the Si-H and Ge-H bonds change respectively.

FTIR absorbance spectra in Figure 3(a) shows incorporation of boron and phosphorous into the SiGe. In the SiGe sample, Si-Si_x-H_y dominates the absorbance around 2080-2150 cm^{-1}.[38] Ge-Ge_x-H_y bonds absorb in the 1975-2000 cm^{-1} range.[29] The peak at 2524 cm^{-1} is attributable to the B-H bond in B_2H_6.[39–41] Boron is seen at 1365 cm^{-1} as either B-

O or amorphous B-H.[39,41] The peak at 1840 cm^{-1} has been described as likely being Si-B_x-H_y,[29] and the peak at 2279 cm^{-1} as Si-P_x-H_y.[38] An oxygen peak around 1050 cm^{-1} indicates mild oxidation of the sample, likely due to tiny leaks in the plasma synthesis reactor or load-lock components.

Figure 3(b) shows DRIFTS of 10% phosphorous-doped $Si_{1-x}Ge_x$ for the full range of x=0 to x=1 in 0.1 increments. While some literature suggests that phosphorous and germanium compete for incorporation into silicon particles, both P and Ge bonds are qualitatively visible throughout the full range of compositions. A slight localized surface plasmon resonance (LSPR) skews the spectra in the lower wavenumbers of the silicon-dominant samples, but it is extinguished by x=0.5 and does not persist into the germanium-rich samples.[42] The LSPR is consistent with other research within the Kortshagen Group and has been reproduced in multiple data sets.

An oxidation study to determine sample stability was performed by placing the DRIFTS accessory in atmosphere and recording spectra over a period of 60 hours post-synthesis. The FTIR spectra, shown in Figure 4, appears to show a slow, steady oxidation over the 2.5 days in atmosphere. However, plotting the ratio of silicon hydrides to germanium hydrides to oxides tells a different story. The oxide to hydride ratio increases rapidly over the first few hours. Hydrogen termination is either replaced by oxygen bonds, or the samples were not fully hydrogen-passivated during synthesis leaving dangling bonds. The oxides overtake both hydride groups after about 8 hours, as shown in Figure 5. These results demonstrate that samples are not air stable and should be kept in an oxygen-free environment, and any post-synthesis treatments should be applied immediately.

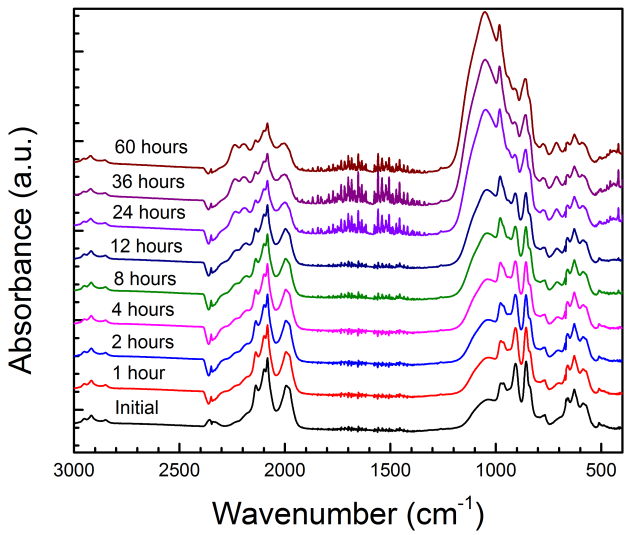

Figure 4: FTIR oxidation study. FTIR absorbance of $Si_{0.8}Ge_{0.2}$ films deposited on aluminum-coated wafer oxidizing over a period of 2.5 days. Spectra are offset for clarity.

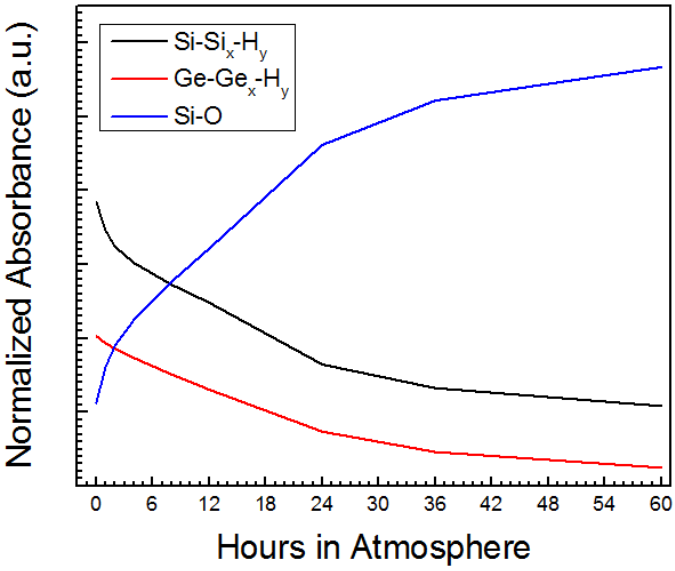

Figure 5: FTIR hydride to oxide ratios. Ratios of silicon hydride, germanium hydride, and oxides plotted against each other over an oxidation period of 2.5 days in atmosphere.

2.6 SCANNING TRANSMISSION ELECTRON MICROSCOPY AND ELECTRON DISPERSIVE X-RAY SPECTROSCOPY

SiGe nanoparticles were also characterized using scanning transmission electron microscopy (STEM) to verify uniformity of particle size, composition, and crystallinity. Undoped SiGe nanoparticles were deposited on holey carbon by inertial impaction via a single swipe under the nanoparticle stream. Imaging was performed by Jacob Held of the Mkhoyan Group at the University of Minnesota on an FEI Titan G2 60-300 STEM operating at 60 keV, 28 mrad convergence angle, 1.3 Å spatial resolution, 100 pA beam current. High angle annular dark field (HAADF) images were taken simultaneously with electron dispersive x-ray (EDX) maps.

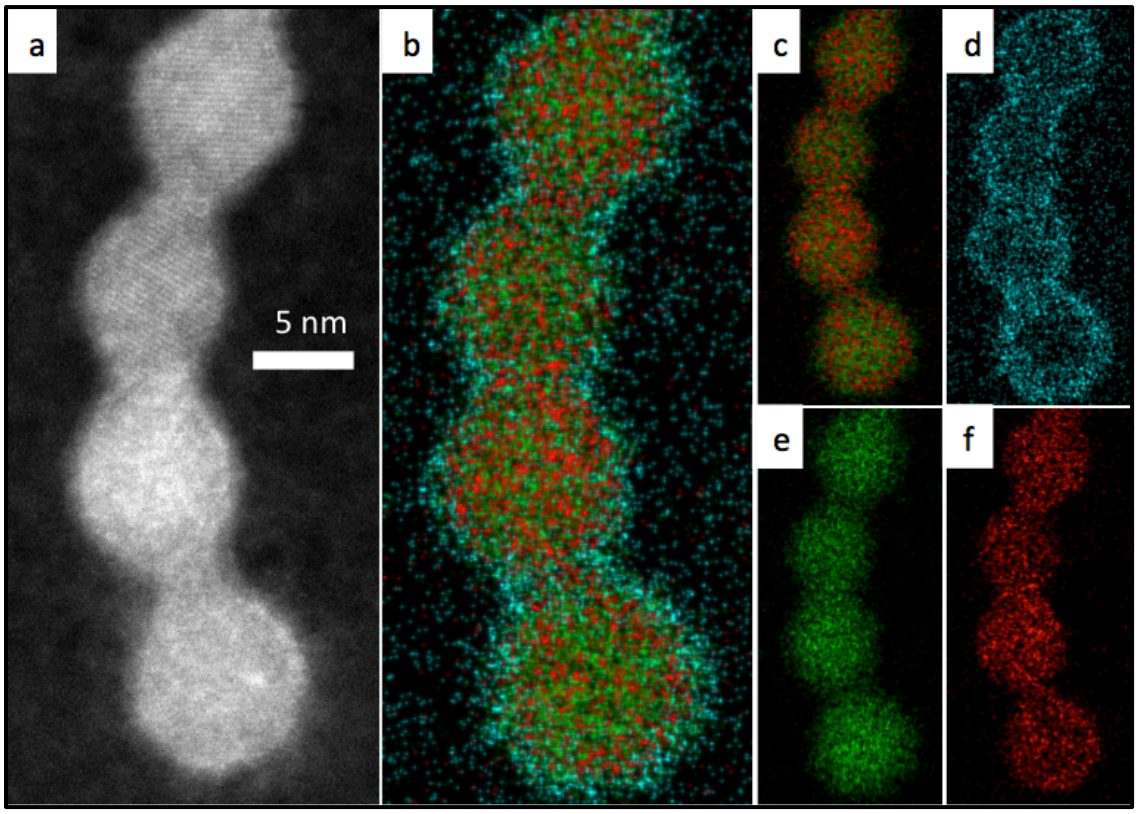

Figure 6: STEM and EDX of SiGe. (a) HAADF-image of several joined SiGe nanoparticles. The top two particles are in focus to see the crystal lattice fringes. (b) Composite EDX maps of the silicon (green),

germanium (red), oxygen (blue) show oxidized particles and a good alloy with no core/shell behavior, as also seen in (c). (d) Oxygen coats the surface of the particles. (e) Silicon and (f) germanium are evenly dispersed throughout the nanoparticles. Images courtesy of Jacob Held.

HAADF images showed that the majority of particles were around 8 nm in diameter though a range of sizes 2 nm – 12 nm were present. The results were consistent with the crystallite diameters measured in XRD. Lattice fringes could be seen on the nanoparticles confirming crystallinity. Many particles formed linear chains of two to six particles (Figure 6), although a lattice mismatch is visible indicating these were formed as individual particles.

EDX mapping images are shown in Figure 6 (b)-(f). Silicon is represented by green pixels, germanium by red, and oxygen by blue in the maps. The nanoparticles were transferred in a load-lock filled with nitrogen from the synthesis reactor to the FEI Titan imaging room. They remained in the load-lock for roughly 1.5 hours and were quickly transferred through atmosphere into FEI Titan and placed under vacuum. Significant surface oxidation is seen on the particles. It is unclear whether this is solely from the transfer period in atmosphere or if the load-lock was not entirely airtight. Silicon and germanium are both seen throughout the particles, proving further that elements are alloyed and no core/shell differences are visible.

One of the largest particles, over 10 nm in diameter, was examined to determine the radial distribution of silicon, germanium, and oxygen (Figure 7). Silicon and germanium are again present throughout the particle. There does appear to be a very thin (Angstrom-order) layer of only silicon on the surface of the particle, which could be a single layer of SiO_2.

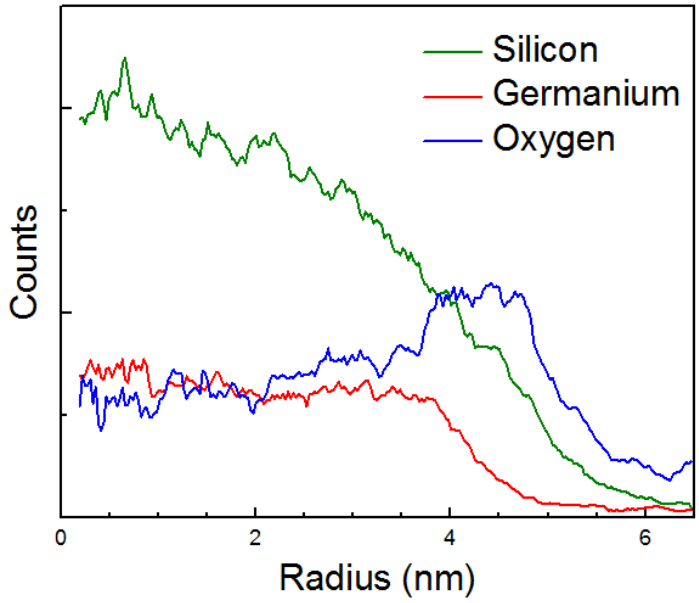

Figure 7: EDX Radial distribution of an SiGe NC with an oxidized surface. EDX data courtesy of Jacob Held.

2.7 CHARACTERIZATION CONCLUSIONS

Successful synthesis of alloyed silicon germanium nanoparticles in tunable compositions was achieved. The nanoparticles are fairly monodisperse and range from 7 – 9 nm depending on synthesis conditions. Samples can be doped with boron or phosphorous to high levels. The samples oxidize quickly, and should always be stored in minimal oxygen environments. Post-synthesis treatments should be applied as soon as possible to avoid oxidation over time, even in low-oxygen environments.

CHAPTER 3: DENSIFICATION TECHNIQUES

3.1 INCREASING ELECTRICAL CONDUCTIVITY THROUGH DENSITY

Inertial impaction of plasma-synthesized nanocrystals does not produce 100% dense samples. Thin films of germanium nanoparticles made on a similar system have been shown to reach up to 60% of bulk density.[31] However, the germanium work was done with the aid of a turbo pump to reduce downstream pressure and increase nanoparticle velocity at the nozzle exit. Further, silicon is lighter than germanium, so SiGe particles impact with less momentum. Thus, the SiGe films produced will have much lower density than 60%. Films with such low density will obviously have very low electrical conductivity. The lattice mismatches in nanostructured samples also reduce electrical conductivity.[25,43,44] Electrical conductivity of the as-produced samples must be enhanced by improving the contact between nanoparticles in the sample through densification and sintering.

Sintering is a metallurgy term used to discuss forming a single body out of a powder without melting the material.[3,45] In the case of SiGe nanoparticles, this means forming a coherent solid for good electron transport while maintaining the grain boundaries and lattice mismatch of the nanoparticles to lower lattice thermal conductivity. Three common methods of sintering were explored – pressureless (heat) sintering, hot pressing (elevated heat and pressure), and cold pressing (high pressure at ambient temperature). Diffusion across grain boundaries is the sintering mechanism for all three methods.[3] Grain growth begins as more diffusion occurs and negates the improvement in thermal properties. To prevent this, heat, pressure, and sintering time must be limited.

Nearly all of the literature on nanostructured SiGe includes ball milling it into a powder and pressure or heat sintering it to near 100% of bulk density.[20,21,25,46] For large thermoelectric generators, such as the ones in spacecraft, a large amount of material is necessary. When targeting these applications, materials are pressed into thick pellets for characterization. However, thin films of $Si_{0.8}Ge_{0.2}$ have attracted interest for potential applications in microthermoelectric devices.[47] SiGe nanopowders were collected for

sintering via cold and hot pressing, and thin films were deposited for pressureless rapid thermal annealing and intense pulsed light sintering experiments. Thin film samples were also made for laser sintering studies performed in collaboration with the University of Virginia.

3.2 RAPID THERMAL ANNEALING

Very little work has been done to sinter crystalline nanoparticles using rapid thermal annealing. More commonly, rapid thermal annealing (RTA) has been used to crystallize amorphous sputtered or ion-implanted materials[48–50], activate dopants in silicon[51,52], or in the fabrication of transistors[53]. Previous work by the Kortshagen group examined RTA of plasma synthesized silicon nanocrystals[54], but silicon germanium alloyed nanocrystals were not investigated.

A Modular Process Technology Corp. RTP-600S rapid thermal annealer was used to investigate heat sintering of 8 nm $Si_{0.8}Ge_{0.2}$. The RTA uses a tungsten-halogen lamp to heat the sample with infrared radiation at a peak wavelength around 1.2 μm. Temperatures up to 1400°C can be achieved, with the substrate wafer temperature measured by a pyrometer.

At high temperatures, staff responsible for the RTA recommended a minimum gas flow of 7 liters per minute (lpm) to prevent overheating in the furnace. The gas flow also serves to purge atmospheric gases from the furnace before it heats up. Nitrogen, forming gas (nitrogen with 5% hydrogen), argon, argon with 5% hydrogen, and nitrogen with 10% oxygen are available to flow during the heating process. The furnace is purged with nitrogen again after the heating period.

Thick films of around 50 μm of undoped SiGe were deposited on an uncoated boron-doped silicon wafer. Substrates were cut very roughly with a scribe to about 8 mm by 10 mm. Experiments did not show deviations in the sample size to be influential on grain growth. The 50 μm film thickness was experimentally determined to provide an accurate measurement of XRD grain size and two-theta position when silicon substrates were compared to microscope slide glass substrates. Glass is not allowed in the RTA due to its low softening temperature

and could not be used as a substrate in this work. Additionally, the thermal conductivity of silicon is three orders of magnitude higher than that of glass or quartz, making it better suited for thermal annealing.

The samples were placed in the RTA on a silicon wafer to hold them in place. Samples placed in different areas of the RTA did not show any difference in characterization. The furnace was initially purged with 7 lpm of nitrogen for two minutes. The temperature was then ramped up to maximum temperature over a period of 30 seconds. Samples were held at maximum temperature for 15 seconds. Two samples were held at maximum temperature for 30 seconds to compare grain growth with respect to hold time. 7 lpm of nitrogen, forming gas, argon, or argon with 5% hydrogen flowed during the high temperature hold time. The furnace was then cooled for 25 seconds under 7 lpm of nitrogen followed by a two-minute, 15 lpm purge with more nitrogen before removal. Samples were transferred into and out of the RTA in atmosphere, so some oxidation resulted.

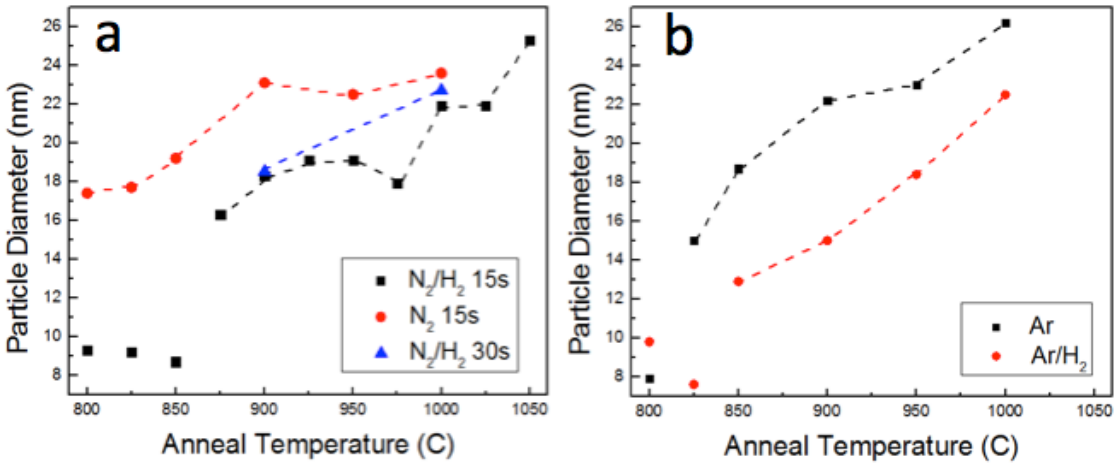

Figure 8: Grain growth of RTA SiGe. Grain size, as determined by XRD, of 50 µm SiGe films after rapid thermal annealing from 800° to 1000°C. Grain size increases with increased temperature but hold time at that temperature is not as influential. Inhomogeneities in this data suggest that grain growth is sensitive to annealing gas and either to sample density or thickness.

XRD measured using the same procedure described in section 2.3, was used to determine if grain growth had occurred. Figure 8 shows that greater grain growth occurred in samples with solely inert gas flowing during the heating period. Samples annealed for 30

seconds exhibited only slightly larger grain growth than those held for 15 seconds. Several points depart from general trends of the grain growth plot. These films may have had slightly different densities or thicknesses than the others resulting from imperfections in the manual film rastering process.

Images of annealed films were taken using a JEOL 6500 Field Emission Gun Scanning Electron Microscope (SEM). Most images were taken at 5 V and 65 µA. Images of inertially impacted films are seen in Figure 9 (a) before annealing at 1050°C and (b) after annealing. The film is very fluffy before annealing and becomes cracked with features on the order of 10-100 µm after annealing. In order to improve impaction, a spacer was added to the pushrod on the load-lock system that attaches to the reactor system, moving the substrate 4 mm closer to the nozzle, to a standoff distance of 1 cm. More uniform films were observed under SEM at this distance. All future films in this work incorporate the spacer to improve film impaction. Figure 9 (c) shows the unannealed film and (d) shows an annealed film deposited using the spacer.

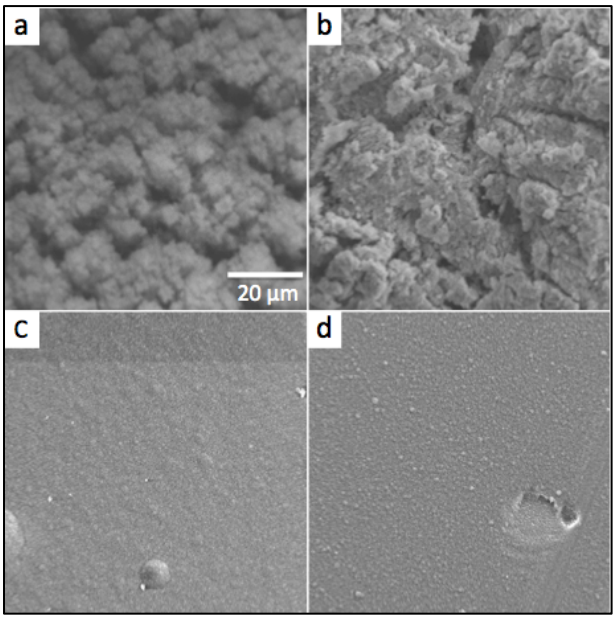

Figure 9: SEM of films with and without a spacer. (a) SiGe film before annealing without spacer. (b) SiGe film without spacer after annealing at 1050°C. (c) SiGe film made using a 14 mm diameter spacer before annealing, and (d) SiGe film after annealing with spacer. Scale bar applies to all images.

To determine whether annealing had densified the films, pre- and post-annealed samples were characterized with ellipsometry. A J.A. Woollam Co Inc EC110 Multi-Wavelength Ellipsometer Control Module with a Chiu Technical Corporation 75W Xenon and 100W Mercury lamp was used in conjunction with WVASE software for ellipsometric analysis. The ellipsometer was located in Professor Eray Aydil's Photovoltaics Group lab. Scans angles were set to the maximum possible values of -90 to 90 and a wavelength of 124 nm – 200 μm so that the scan parameters were limited only by the equipment. An effective medium approximation model was made with SiGe and void spaces. Density and thickness were fit automatically in the software from the data, using the estimated thickness based on nanoparticle deposition time as a starting point. The software reports a mean squared error based on the fit of the model to the data collected. These fits were qualitatively poor, but reasonable trends emerged from the data. It is likely that the error in these measurements is higher than the software reported due to the imperfect modeling technique.

Table 3: Ellipsometric fits of density and thickness on samples after rapid thermal annealing.

Anneal Temperature (C)	Location	Density (% of bulk)	Density Error	Thickness (nm)	Thickness Error (nm)	Mean Squared Error
Not Annealed	Center	14.3	0.3	3935	57	7.0
800	Center	28.2	0.5	2483	37	5.2
850	Center	24.2	1.6	2555	143	8.2
900	Center	26.9	0.4	2586	32	7.9
900	Periphery	11.7	0.4	3690	66	9.2
950	Center	27.7	0.3	2601	21	8.0
950	Periphery	18.3	1.5	2911	166	10.8

Ellipsometric data show that density increases and thickness decreases in all annealed samples. The results also indicate that the outer edges of the films, labeled "Periphery" in Table 3, are much lower density than those in the middle of the film, labeled "Center". The

thickness of the unannealed sample is in line with the expected result. After annealing, all samples are roughly half the thickness and double the density of the unannealed sample. While the error on these fits is admittedly high, it does demonstrate that increasing grain growth by increasing temperature does not necessarily increase densification. This gives further evidence that temperature increases in excess of the point where grain growth begins to occur are not desirable or necessary.

Unfortunately, during the course of this research, the ellipsometer was rendered inoperable and could not be used for further research. Similar analysis was attempted on a V-VASE Spectroscopic Ellipsometer with WVASE32 software. Acceptable fits could not be achieved on this device with the models available.

3.3 HYDROGEN REMOVAL

Before moving on to hot-pressing, it was necessary to address issues of sample cracking observed in prior work within this research group.[55] Plasma-synthesized silicon nanoparticles were hot-pressed in previous research but many of the samples exhibited cracking indicative of hydrogen embrittlement. Hydrogen embrittlement is a common problem in metals, where excess hydrogen combines into H_2 to form planes of molecular hydrogen, that cause cracks in the material. It was hypothesized that the cracking seen in previous research was caused in part by hydrogen termination of the silicon nanocrystals.

Samples were subjected to a heat treatment to determine at what temperature the hydrogen would be removed. Films of about 10 microns were deposited on silicon wafer. For this experiment, FTIR had to be done with a transmission accessory. DRIFTS could not be done since a reflective coating, such as the aluminum-coated substrates described in Chapter 2.5, is required. Silicon and aluminum alloy into a eutectic material that melts at temperatures as low as 577°C. Even if this point is not reached, significant contamination can result as aluminum diffuses into the silicon at increased temperatures.

Samples were placed on a hot plate in a nitrogen-purged glovebox and heated quickly to maximum temperatures of 200, 300, and 400°C. Two samples were place on the hot plate

for each temperature. Maximum temperature was reached within 2-5 minutes, held for 30 seconds, and the first sample was removed and set on a piece of aluminum foil to cool. The second sample was removed after being at maximum temperature for 5 minutes. Samples were compared in transmission FTIR after full cooling. The quick purge function on the glove box was turned on during heating to prevent the glovebox from becoming dangerously hot. This provided a nitrogen flow over the samples to carry away H_2 being released from the samples. However, the flow was minimal. Immediately after this procedure, any use of the glovebox antechambers gave off a strong odor, signifying appreciable outgassing from the sample during heating.

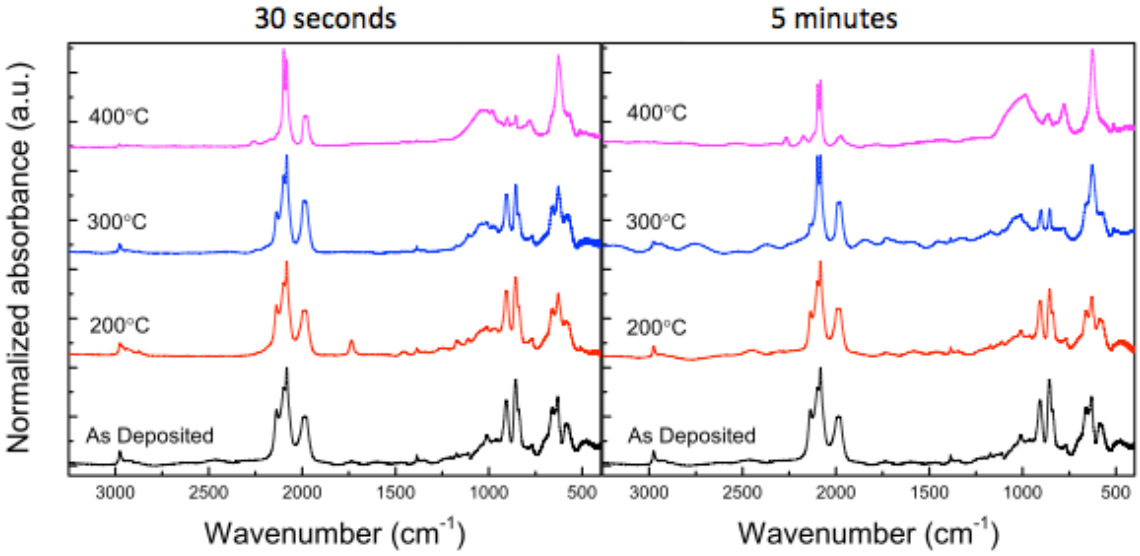

Figure 10: FTIR of hot plate hydrogen removal. Thin films placed on a hot plate in a nitrogen-purged glovebox for 30 seconds (left) and 5 minutes (right). Changes in the hydride signals are visible in 300°C after 5 minutes and 400°C after 30 seconds and 5 minutes.

A similar experiment was done in the rapid thermal annealer where the nitrogen flow was set to 7 liters per minute to purge the furnace of H_2 and other molecules emanating from the sample as it heated. Samples were heated to 200, 300, 400, and 800°C for 30 seconds and 400°C for 5 minutes. Samples were transferred into and out of the RTA in atmosphere, so additional oxidation is seen in the FTIR. More degradation of the hydride peaks are seen in

the RTA-treated samples than the hot plate-treated samples. This could be a result of more complete heating in the RTA than on the hot plate. The hot plate only heats the sample from below, meaning heat must be transferred through the substrate to the film. The RTA heats the sample uniformly around the sample, and more directly reaches the nanoparticle film. It could also be a result of the increased nitrogen flow removing outgassed molecules from the furnace.

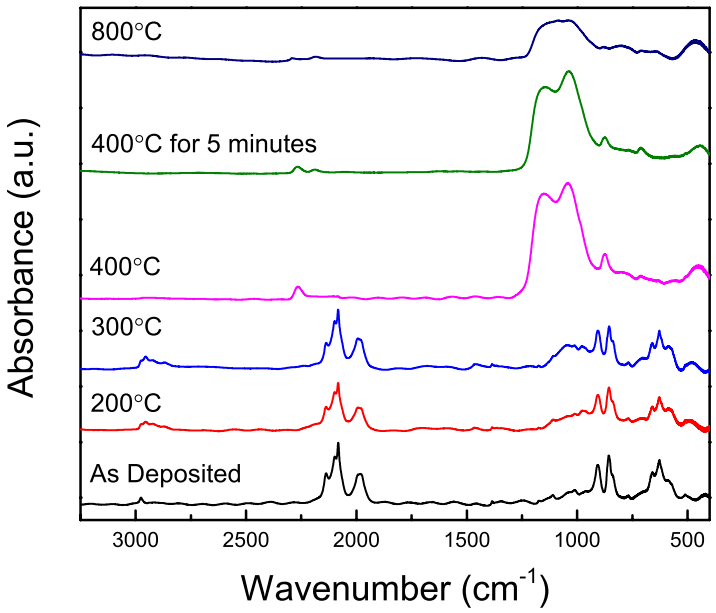

Figure 11: FTIR of RTA hydrogen removal. Thin films placed in the rapid thermal annealer and left at maximum temperature for 30 seconds and one sample for 5 minutes to match the conditions of the hot plate experiment.

In both the hot-plate treated and rapid thermal annealed samples, 30 seconds at 400°C removes some to most of the hydrogen from the nanoparticles. With this temperature as a target, nanoparticle powders were heat-treated in a Lindberg model 55035 tube furnace with a steady nitrogen flow over the particles. Powders were placed in an alumina combustion boat inside a 25 mm outer diameter fused quartz tube. Lines were plumbed from the

laboratory nitrogen supply, and a mass flow controller was connected to limit flow to the tube furnace. The tube furnace outlet was connected to the laboratory exhaust system to prevent outgassing from entering the workspace air.

Nitrogen flow was set to 1370 sccm, the maximum possible flow rate for the mass flow controller. The system was calibrated using a thermocouple inside the tube to determine the relationship between the internal temperature and the temperature applied to the tube as displayed on the furnace. The internal temperature was 83% of the external readout at temperatures above 250°C. Nanopowders were heated to an external readout temperature of 482°C in accordance with the calibration. FTIR of an annealed sample confirmed the hydride peaks were no longer present after treatment.

A pushrod assembly was constructed to transfer the nanopowders in and out of the tube furnace without exposing them to atmosphere. Nanoparticle powders were placed in a custom-formed fused quartz boat made of a cylinder with one end open in a half circle as shown in Figure 12. A small rod was connected to the outer diameter of the pushrod assembly that connected to an air-free loadlock. As the pushrod was rotated, the outer diameter rod moved higher and lower, allowing it to pick up and drop off the boat in the quartz tube. While the mechanism worked well for some runs, on others the boat would get stuck due to a misalignment problem with the tube and break. Fused quartz was not an ideal material for the boat because static charge would build up and repel the nanoparticles so that they would not stay in the boat. This design would have to be modified for more reliable use. Many runs of the tube furnace were used without it. An alumina combustion boat was used instead. On these runs, the particles were transferred in air, allowing them to oxidize briefly as they were loaded in and out.

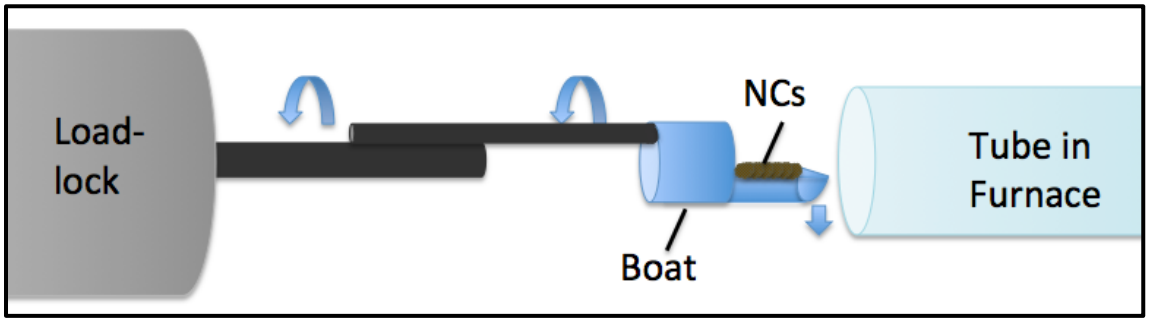

Figure 12: Schematic of air-free loadlock for powder transfer. Misalignment issues caused it to be unreliable.

3.4 HOT PRESSING

SiGe powders were collected to assess hot pressing as a compaction method. A hot press die was machined out of Poco HPD-1 graphite. The die body measured 15 mm in height with a 7.92 mm hole bored out. Two 7.5 mm-long pistons fit in the hole with 5 mm ends matching the width of the die body for easier powder loading, as pictured in Figure 13. The die was designed to fit into the custom-built hot press system in Professor David Kohlstedt's lab in the Department of Earth Sciences.

The die was placed between two rods in the hot press and axially loaded from pressure on the bottom. A heater surrounding the rods translated up to cover the die when heating and translated down to unload the die.

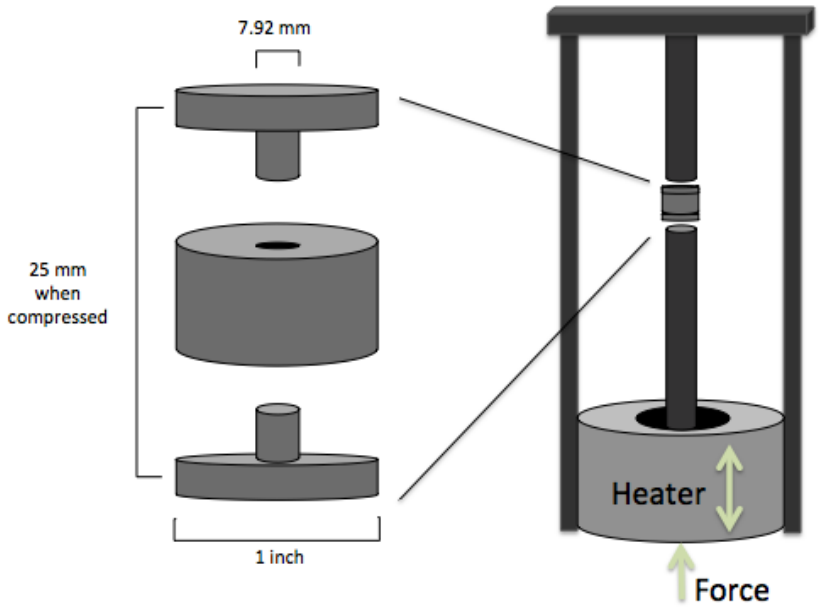

Figure 13: Hot press and die schematic. A hot press die was machined to fit in an axially loaded hot press with a vertically translating heater in the lab of Professor David Kohlstedt, Earth Sciences Department, University of Minnesota.

Argon was flowed through the hot press heating chamber at temperatures up to 2000°C. A maximum pressure of 30 MPa was achieved by loading 100 kg of weights onto a lever below the rig that pressed up on the axial bars holding the die in place.

To hot press a 1 mm pellet to 100% of bulk density, it was calculated that 148.2 mg of nanopowder would be needed. Losses during tube-furnace pre-treatments and during die loading dictated that 175 mg of SiGe nanoparticles should be synthesized for each run. To speed up particle collection, synthesis recipes with higher precursor flow rates were tested. A concern with increasing flow rate was that nanoparticles would be amorphous, germanium incorporation would not scale, or the nanoparticle diameter would change by decreasing the residence (formation) time in the plasma.

Powders were synthesized at the normal recipe as listed in Table 1, 1.5 times the precursors at the same 110 W power, 2 times the precursors at 100 W, and 2 times the precursors at 130 W. Nanopowder yield scaled approximately with the precursor flow rate increases. XRD was used to characterize the size, crystallinity, and composition.

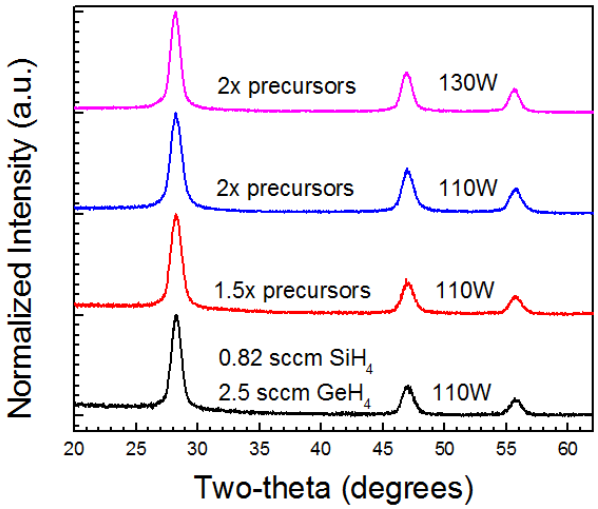

Figure 14: XRD of high-yield recipes. Crystallinity and composition show no change with precursor flow rate scaling.

Table 4: Nanocrystal diameter in scaled-up recipes.

Precursor Flow	Power	NC Diameter
1x	110 W	9 nm
1.5x	110 W	8.2 nm
2x	110 W	8 nm
2x	130 W	9.5 nm

Figure 14 shows that no change in crystallinity or two-theta peak position are visible in XRD of the scaled-up recipes. Table 4, however, shows size changes with precursor and power change. The regular recipe particles were slightly larger than normal at about 9 nm in diameter. This is likely the result of the nozzle being set smaller than usual. At a constant power, particle size decreases with increased precursor flow. Increasing the power to 130 W at double the flow rates increases particle size to 9.5 nm.

While these results were encouraging from a particle synthesis viewpoint, practical considerations made higher flow rates and yield recipes less attractive once attempted at a full deposition length. With increased flow rates, the nozzle between the plasma and the collection substrate would clog more quickly causing the pressure in the plasma region to spike rapidly. Since this affects nanoparticle synthesis, the gases had to be turned off and the nozzle unclogged by purging high-pressure nitrogen through the nozzle. The increased time

used in multiple purges negated any time saved in depositing a higher yield. Powders collected after this point continued to use the normal recipe.

Although the increased yield recipes were not useful for this particular research, the scalability of the recipe is very interesting for future synthesis. If a nozzle was designed with smoother flow to decrease particle deposition on the components, clogging would not occur, and a higher yield could be achieved. This has clear implications for scalability in industry, where large yields would be a prerequisite for commercial nanoparticle synthesis.

Once nanopowders were collected, they were transferred to the tube furnace for hydrogen removal. Some samples were not subjected to the tube furnace heat treatment for comparison to heat-treated samples. The powders were then packed into the graphite die, which was in turn sealed in a vacuum bag for transport to the hot press.

Samples were transferred out of the vacuum bag and into the hot press in atmosphere. Weights were loaded to apply 20-30 MPa to the die. Most samples were heated with a ramp rate of 8°C per minute. Samples were held at maximum temperature for 1-60 minutes. At this point, during some trials, the weights were unloaded before cooling. In other trials, the weights were left on to continue applying pressure until the sample was completely cool. Weight removal did not produce noticeable differences in final pressed samples. The system was shut off after the hold at maximum temperature and allowed to cool as quickly as possible. One sample was ramped down over night to ensure that thermal shock effects were not causing fracturing.

Initial hot pressing runs were attempted at 20 MPa, producing 30% dense pellets. To increase density, a cold press step was added, since cold pressing could be done at much higher pressures, and hot-press pressures were increased to the maximum possible pressure of 30 MPa. Cold pressing at 100 MPa did not produce a coherent pellet on its own and could not be used as a stand-alone sintering method. At higher pressures, cold pressing commonly caused the die piston to fracture and ruin the sample. Literature suggests cold-pressing SiGe requires upwards of 490MPa to reach bulk density.[56] A steel die would need to be fabricated to achieve such high pressures.

Results of hot pressing were extremely inconsistent. Nearly all of the samples fractured and broke into small pieces upon removal from the die. Samples that had not been subjected to tube-furnace hydrogen removal exhibited a unique cuboid cracking pattern. The sample broke vertically into many similar sized cuboid pieces. One of these pieces is shown in Figure 15.

Figure 15: Photographs of a cuboid piece from fractured SiGe pellet.

Samples that had the hydrogen removed from the nanoparticle surface also experienced cracking, but the cracking had no preferred direction. These samples were more robust than the samples of hydrogen-terminated particles and did not tend to break immediately upon removal from the die. They were still likely to crack over time and break during handling.

Density of the compacted pellets was low. Most densities ranged from 30%-57%, and this density was not correlated with the hot press conditions. Either the die piston or the pellet would routinely get stuck in the die body, preventing full densification and removal of the pellet. A graphite lubricant, a boron nitride paint lubricant, and a boron nitride spray lubricant were all used on the die and die piston to attempt to prevent cracking. The graphite lubricant was marginally successful in preventing the die piston from sticking to the die body, but did not prevent the pellet from sticking. Both boron nitride lubricants were very thick and actually increased piston sticking by making the piston too large for the hole in the die body.

One broken sample was polished and examined in SEM to better understand why fractures were occurring. The sample broke before an accurate measurement could be taken, but it is estimated that the pellet was around 35% dense. The sample showed several different phases in the material. Figure 16 (a) shows the cuboid fracture pattern of a

hydrogen-terminated sample. Figure 16 (b) shows high magnification of a smaller broken piece of sample with a porous structure.

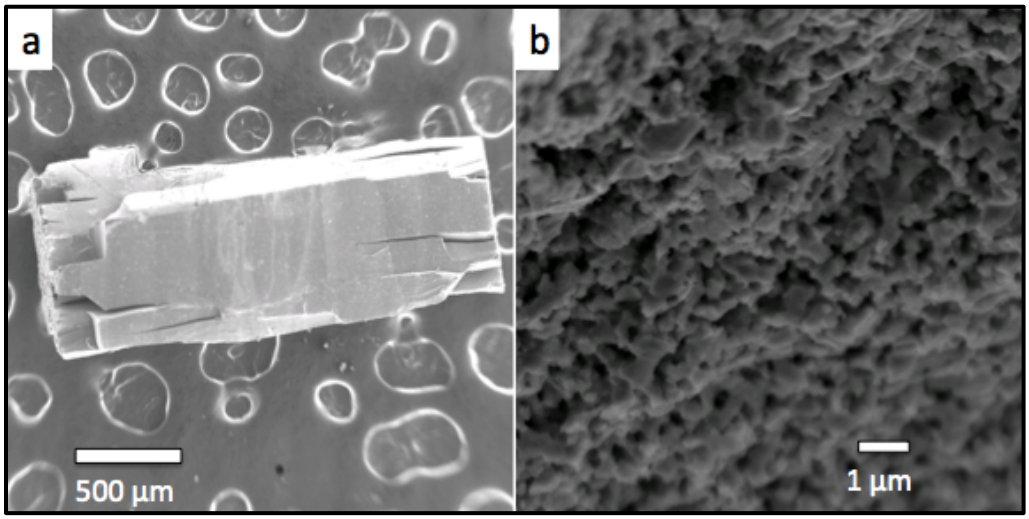

Figure 16: SEM of fractured hot press pieces. (a) A piece of broken hot pressed pellet sitting on conductive carbon tape is further fracturing into cuboids. (b) A piece of pellet broken to be smaller shows a highly porous structure under SEM.

Figure 17 shows an abrupt change in density and pore size in the compacted particles. Features on the right side of the image are on the nanometer scale while features on the left are microns in size. The cause of this phase difference is unknown, but it likely contributes to the sample fracturing. Figure 18 shows these phases under higher magnification.

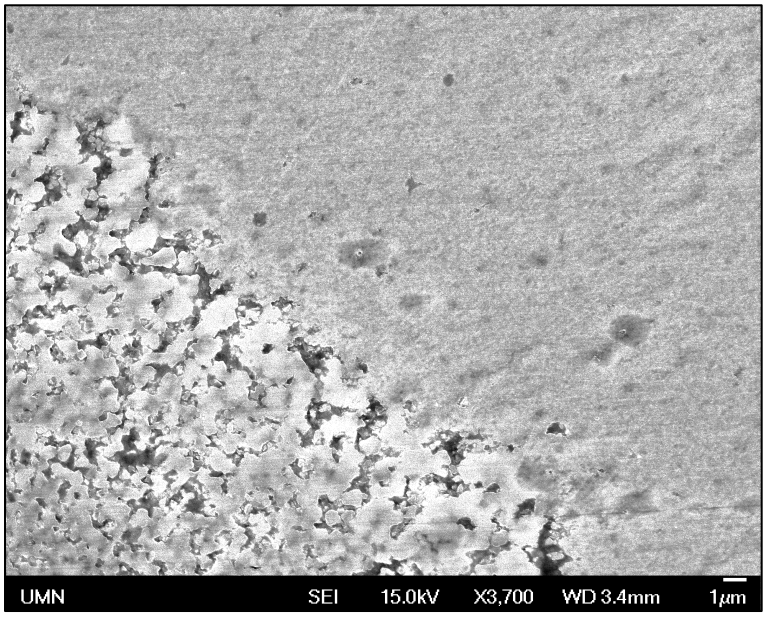

Figure 17: SEM of SiGe phases. A broken pellet shows abrupt changes in pore size in the material that may contribute to fracturing. Image taken by Jacob Held on a JEOL 6700 SEM.

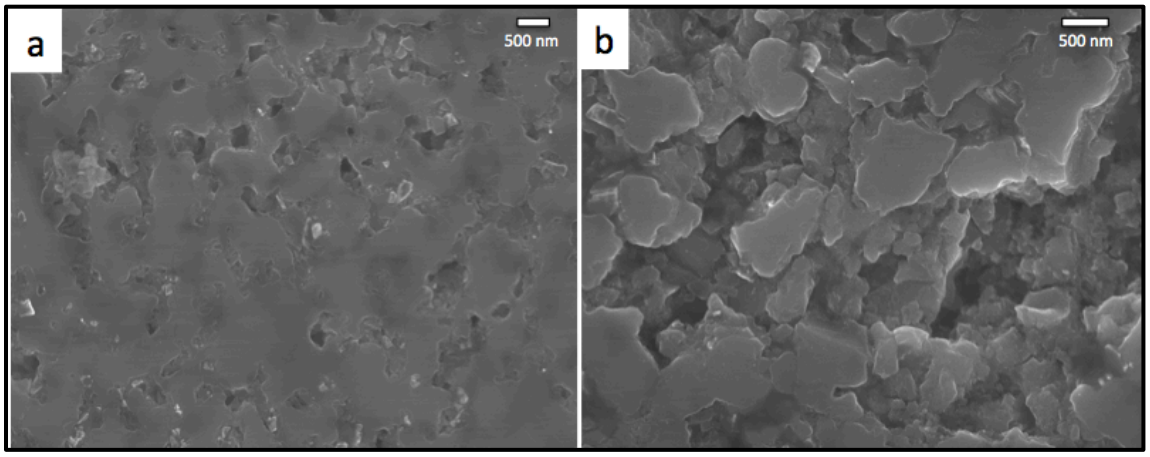

Figure 18: SEM of (a) the more dense part and (b) the less dense part of a compacted SiGe pellet.

The broken pellet was further crushed into a very fine powder in methanol and dip cast onto a holey-carbon TEM grid. TEM was done at 200kV, 32 mrad convergence angle in the FEI Titan as described in section 2.6. Some areas of the sample showed almost no grain

growth but a well-sintered porous structure. Other areas had undergone significant grain growth with grains that appeared over 200 nm wide (Figure 19).

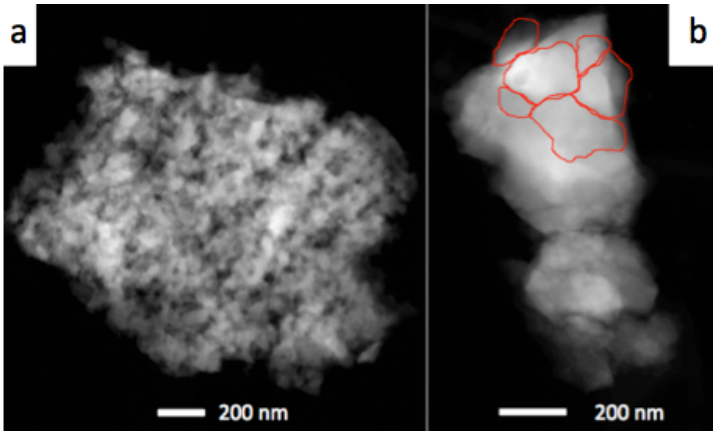

Figure 19: TEM of crushed hot pressed SiGe pellets. Some areas exhibit sintered small nanocrystals (a) and some areas exhibit large single grains grown at high temperature (b). Image courteous of Jacob Held, Mkhoyan Group, University of Minnesota.

In the less dense areas of small nanocrystals, lattice fringes could be seen sintered to one another in random orientations (Figure 20). This phase of the material is very desirable for its lattice mismatch, although still too porous to have good electrical conductivity.

One image of a piece of SiGe, shown in Figure 19 (b), pictured large grains on the top half and sintered small grains on the lower half. An EDX map of the piece of SiGe was taken to see if there was a difference in composition causing grain growth in the top particles and no growth in the bottom ones. EDX revealed a slightly higher concentration of germanium in the area of large grains than in the area of small grains as can be seen visually between the top and bottom portions of Figure 21 (a). This may mean that minute differences in composition cause areas with more germanium to preferentially grow larger grains, since germanium has a lower melting point. The results were not definite enough to be completely certain that this is the cause of the grain size inconsistencies.

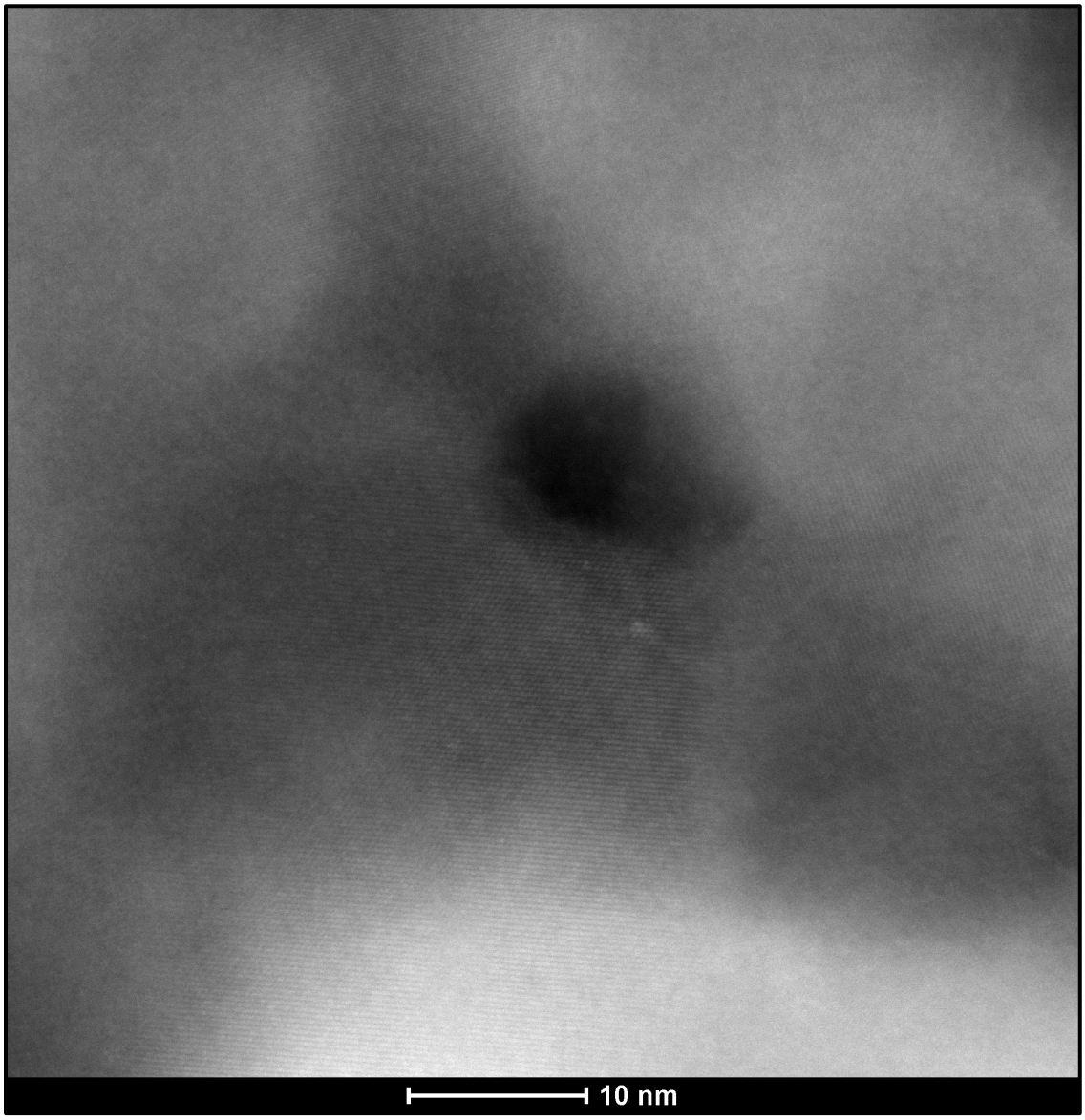

Figure 20: TEM of hot pressed SiGe. Lattice fringes are visible in sintered nanocrystals with random orientation. If higher density was achievable, this result would be ideal for thermoelectric applications. Image courtesy of Jacob Held, Mkhoyan Group, University of Minnesota.

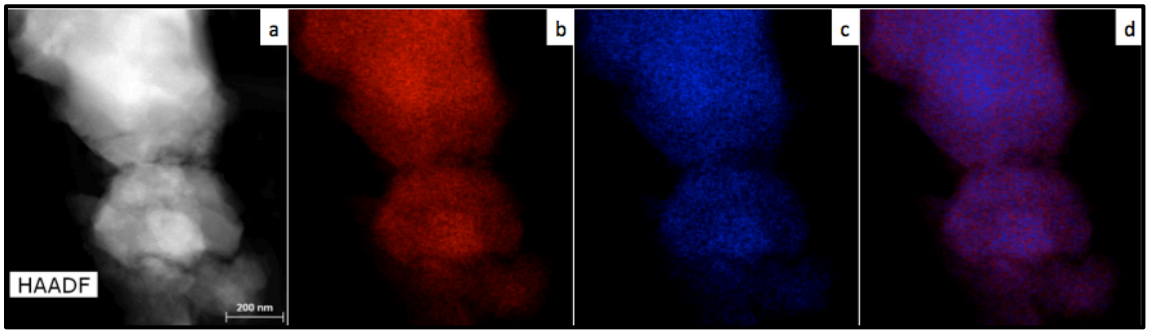

Figure 21: a) HAADF of sintered SiGe particles shows large grains in the upper half of the image and smaller grains in the lower half. EDX maps of silicon (b) and germanium (c) and a silicon and germanium composite image (d) show a slightly higher concentration of germanium in the region where grains are larger. Images courtesy of Jacob Held, Mkhoyan Group, University of Minnesota.

After over a dozen trials exhausting the capabilities of the hot press, it was determined that the available press would not be able to compact the pellets to a high enough density to make good measurements. Only two samples remained intact and were just above 30% dense (Figure 22). Further, six pistons fractured during the research, ruining one in three samples. Successful hot pressing to bulk density in the literature has been at much higher pressures or with the aid of spark plasma sintering.[57] Without the aid of hot press pressures above 100 MPa or cold press pressures of upwards of 500 MPa and a more reliable die, films provide a more robust area for research with comparable densities to the pellets produced here.

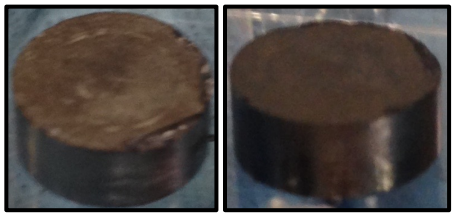

Figure 22: Hot pressed pellets at 30-40% of bulk density.

3.5 LASER ANNEALING

Nanoparticle films were shipped to the University of Virginia in a collaboration to assess the effect of laser annealing on SiGe NC thin-films. 5% nominally phosphorous-doped SiGe films of 3-10 µm were deposited on ½ inch by ¾ inch pieces of fused quartz. They were packed in resealable plastic vacuum bags and excess air was removed from the bag. The samples were shipped overnight to Virginia, where they were removed and placed in a vacuum desiccator until laser treatment was performed.

An IPG Photonics YLR-150 1500 W Quasi Continuous Wave Ytterbium Fiber Laser with a 1070 nm wavelength was used in pulsed mode to treat the SiGe NC films. Treatment is done under argon at 1 atm. The laser beam moves in a line across the sample at 0.5 mm/s (Figure 23a). Up to 7 lines can be made using different parameters on the same sample, making it easy to compare laser parameters without sample variation between synthesis runs playing a role.

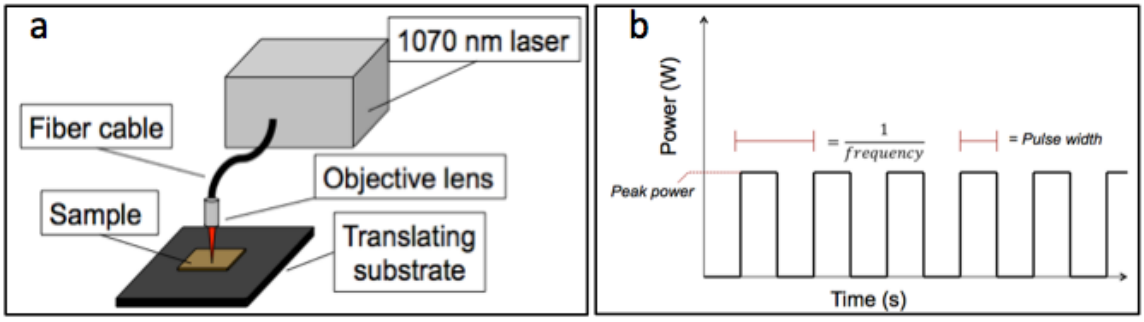

Figure 23: a) Laser annealing is done by placing a sample underneath the 1070 nm laser beam. The sample sits on a translating substrate that moves the sample at 0.5 mm/s, making a line of sintered film. b) Three parameters control the laser pulses – peak power (as a percent of 1500 W), frequency, and pulse width.

The laser was set to a peak power of 15-25% of maximum power (1500 W). 100% of maximum power would melt the sample, so lower powers must be used. For a given pulse width, frequencies of 200-1400 Hz were attempted. By increasing frequency with the same pulse width, the time the laser is off is shortened, imparting more overall energy to the sample.

One film sample was laser annealed at 15% power (225 W), 0.1 ms pulse width in 6 isolated lines from 200-1200 Hz in increments of 200 Hz. SEM on the samples shows large white spots on top of a black background. With increasing frequency, the white areas become larger, indicating percolation effects that increase with energy (Figure 24). This is consistent with germanium percolating to the top of laser annealed samples in research performed with a continuous wave laser in a UMN/UVA collaboration.[54,58] Germanium, having a lower melting point than silicon, is presumably melting and forming beads on the surface that grow as more energy is applied. This is supported by an EDX line scan done across one of the black and white transition areas that confirms that germanium and silicon are segregating (Figure 25).

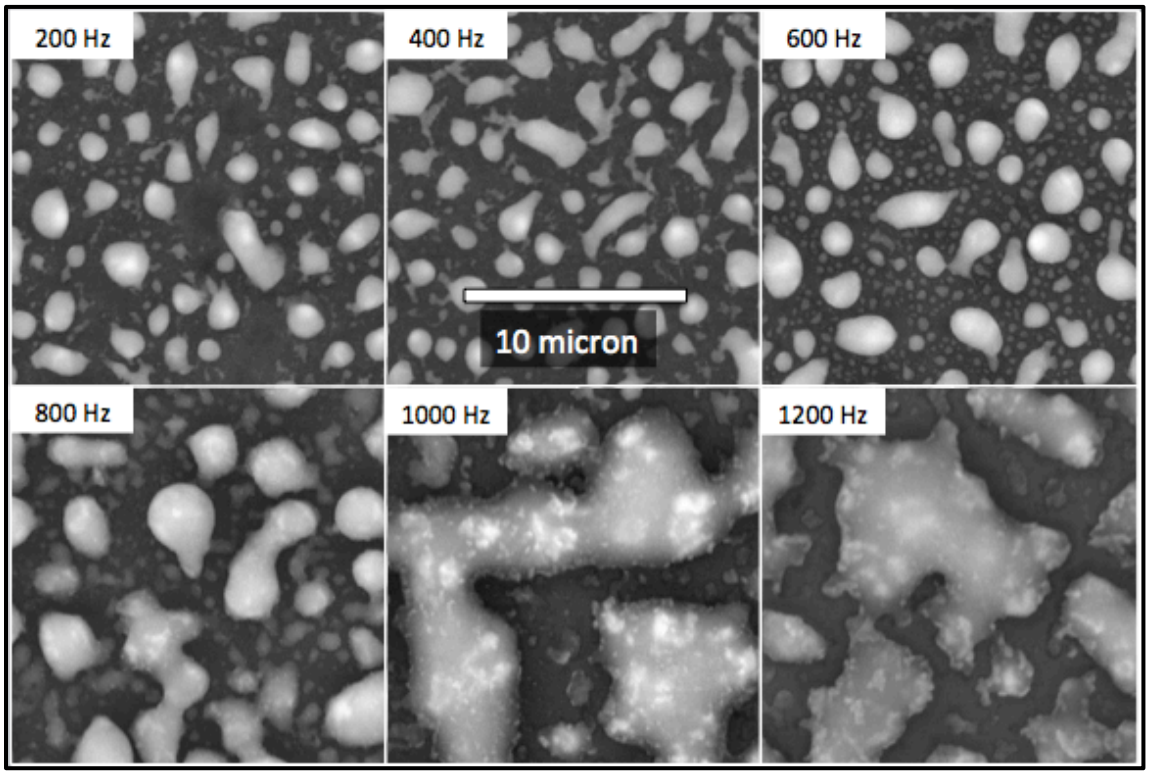

Figure 24: SEM images of 15% peak power, 0.1 ms pulse width laser-sintered SiGe at different frequencies shows significant phase separation attributed to germanium percolation. Samples were deposited on three pieces of 19 mm fused quartz for 1 minute 38 seconds using the n-type recipe listed in Table 1 with 2.6 sccm of germane. This correlates to an expected thickness of around 6 µm. SEM images courtesy of Kai Xie, Gupta group, University of Virginia.

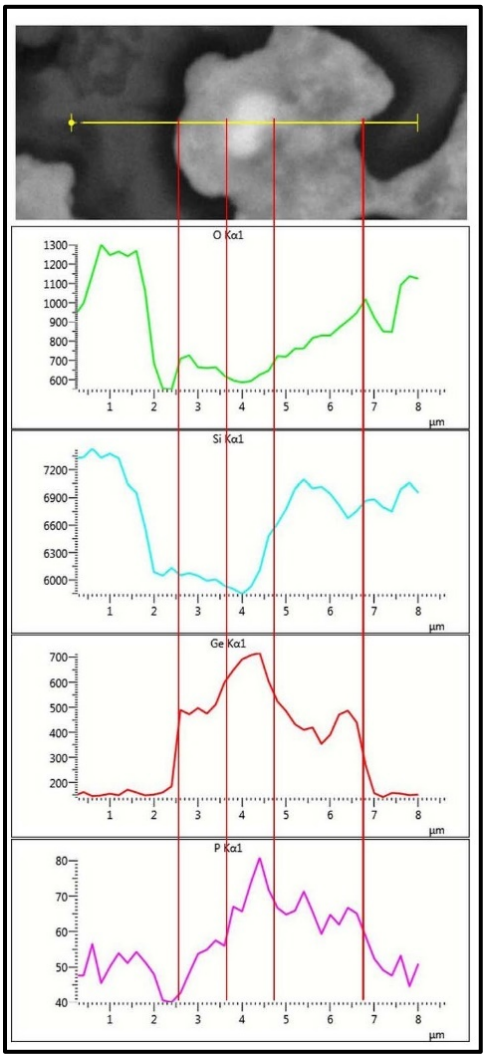

Figure 25: EDX line scan of laser sintered SiGe. Courtesy of Kai Xie, Gupta Group, University of Virginia.

While the presence of a small amount of liquid phase material can allow sintering at lower temperatures,[3] this level of germanium diffusion out of the alloy can be detrimental to the thermoelectric properties. With germanium out of the lattice, the improvement seen

through lower lattice conductivity in the alloy will be lost. Conversely, the electrical properties increase dramatically after the laser treatment.

Another sample with the same deposition parameters was laser annealed at 20% peak power, and electrical resistivity measurements were performed. Figure 24 shows SEM images of samples laser annealed with a 0.1 ms pulse width and frequencies of 200 Hz (a), 400 Hz (b), and 800 Hz (c). The electrical resistivities were measured on a four point probe to be 1.09 Ω*cm, 0.48 Ω* cm, and 0.9 Ω*cm. The maximum conductivity of these samples being at 400 Hz demonstrates that a balance must be struck between imparting enough energy for complete sintering to occur and a low enough energy that the germanium does not completely percolate out of the alloy to the surface of the film.

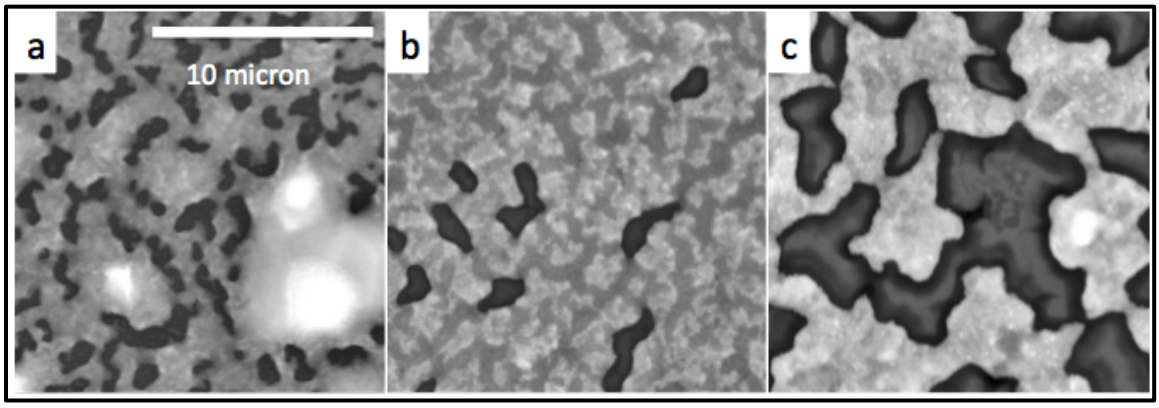

Figure 26: SEM images of laser sintered SiGe at 20% peak power with a 0.1 ms pulse width and a frequency of 200 Hz (a), 400 Hz (b), and 800 Hz (c). Samples were deposited on three 19 mm pieces of fused quartz for 1 minute 38 seconds correlating to an expected thickness of around 6 µm. SEM images courteous of Kai Xie, Gupta Group, University of Virginia.

One problem with this laser sintering method is that the laser has a Gaussian beam. The peak intensity is in the middle of the beam, meaning that the portion of the film treated by the middle of the beam will experience more grain growth than the areas treated by the edge of the beam. An SEM image of this variation is visible in Figure 27.

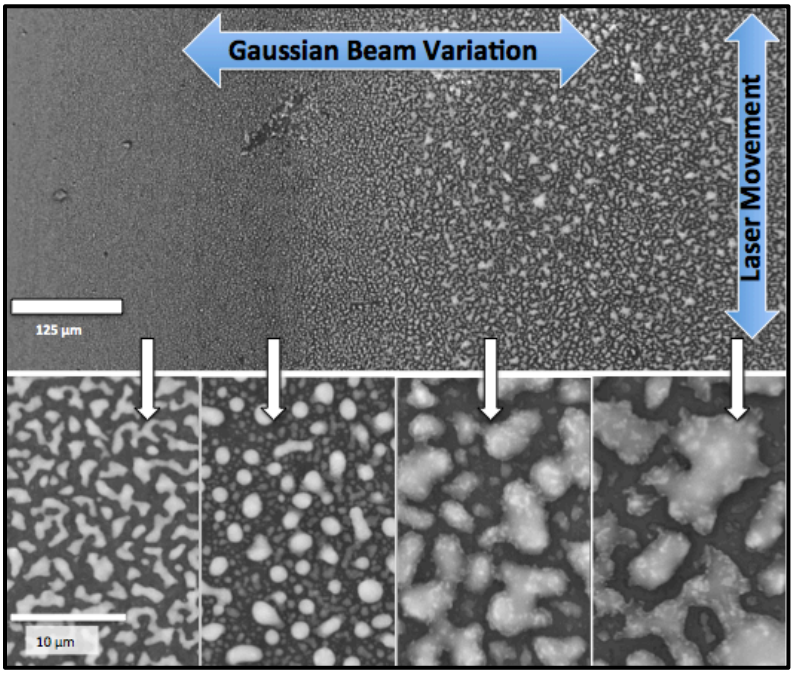

Figure 27: SEM images of a single laser-sintered film shows variations in post-annealed film due to the Gaussian variation in the beam perpendicular to the direction of laser movement during processing. Images were taken by Kai Xie, Gupta Group, University of Virginia.

Laser sintering has been successful in increasing the electrical conductivity of SiGe films. However, without thermal conductivity measurements to discern whether an increase in thermal conductivity is negating the effects of improved electrical conductivity, it is difficult to know whether the laser treatment is increasing the figure of merit. The germanium percolating to the surface is an undesirable effect, and efforts will need to be made to reduce separation of the alloy elements in annealing.

3. 6 INTENSE PULSED LIGHT SINTERING

Intense pulsed light, or photonic, sintering has been used to anneal conducting and semiconducting nanoparticles like copper, silver, copper zinc tin sulfide, and zinc oxide with great success.[59–64] Intense pulsed light (IPL) sintering of silicon nanoparticle inks was

reported, although the process encouraged more melting of the nanoparticles than sintering.[65] IPL treatments are attractive because of their adaptability to roll-to-roll production processes. Thin films could be produced on a roll and sintered with light in seconds. Silicon germanium films would be no exception. With some initial effort, a roll-to-roll process with IPL treatment could be realized in the same laboratory used to plasma-synthesize the nanoparticles researched here. The possibility for performing this treatment under vacuum or inert gas is also of interest, since it could sinter the particles before any oxide layer was to develop and improve electrical properties.

Silicon germanium is more responsive to IPL treatments than silicon, because germanium absorbs at lower energies than silicon does. Figure 28 (a) shows the absorption coefficient of Si, Ge, and several compositions of SiGe.[5] Figure 28 (b) shows the emission spectra for the xenon lamp used in IPL sintering experiments in Professor Lorraine Francis' research group at the University of Minnesota. Most of the xenon lamp emission spectra lies above 350 nm. In this region, the germanium absorption coefficient is much higher than that of silicon.

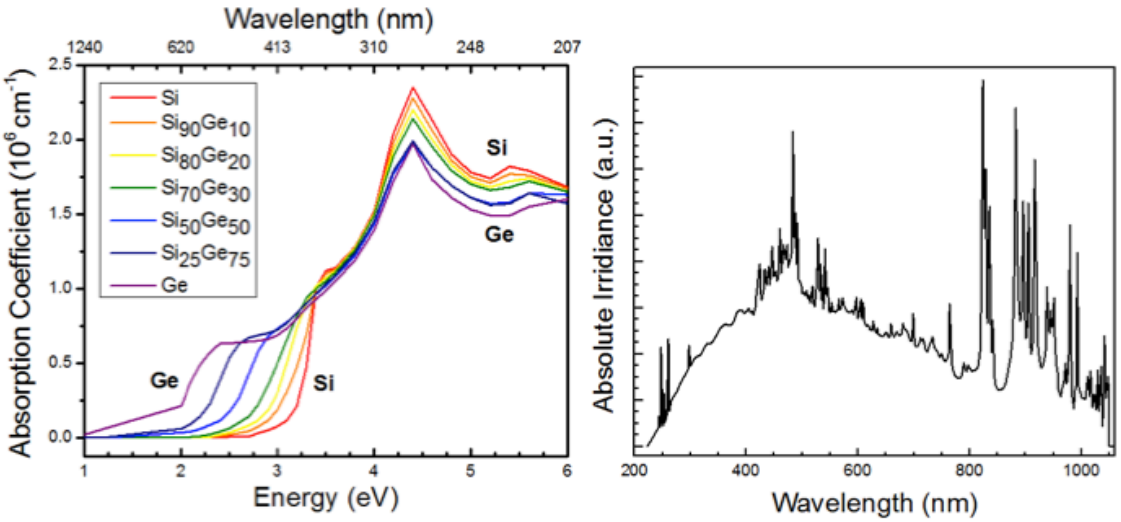

Figure 28: Left: Germanium and alloys of silicon germanium absorb at lower energies than silicon.[5] Right: The Xenon lamp emits primarily in wavelengths where germanium has a higher absorption coefficient than silicon. Germanium will experience greater heating than silicon.

The Xenon Sinteron 2010 lamp in Professor Francis' lab in Chemical Engineering and Materials Science was used to IPL treat plasma-synthesized SiGe films. Films were deposited to be 2-4 μm thick on fused quartz, boron-doped silicon wafer, and undoped silicon wafer with a 300 nm thermal oxide. The lamp is pulsed at 1.9-3 kV for a pulse width of 0.1-3 ms (Figure 29). It was discovered that using too short a period led to the sample overheating and delaminating from the substrate or inducing large grain growth in the sample. Periods of 660 μs to several milliseconds were used to provide cooling time in between pulses. Experience shows that short pulses with long periods provide a superior film morphology after IPL treatment.

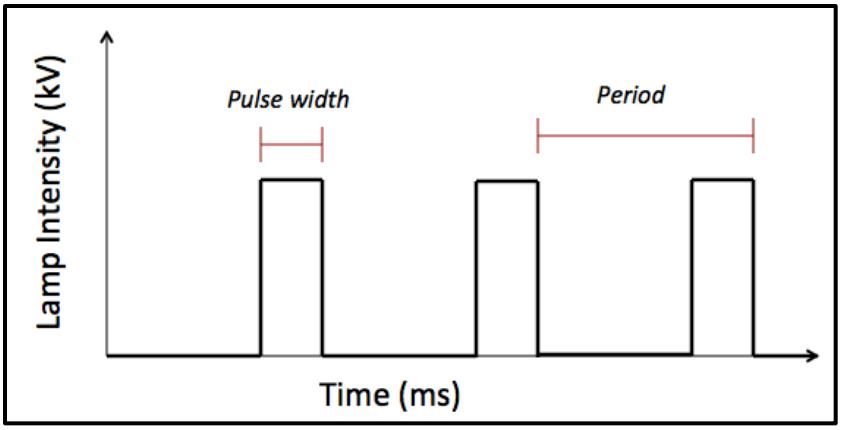

Figure 29: The xenon lamp is pulsed for 0.1-3 ms at a time. The period can be adjusted so that the lamp is off for hundreds of milliseconds in between pulses, allowing the sample to cool so that the germanium is less likely to diffuse out of the film.

FTIR was done on an SiGe sample on aluminum coated wafer that was IPL treated at 3 kV for a single 1 ms pulse. Figure 30 shows that the hydride bonds have been removed during this process. The remaining large peak appears to be an oxide peak. The treatment was done in atmosphere and significant oxidation is likely to have occurred.

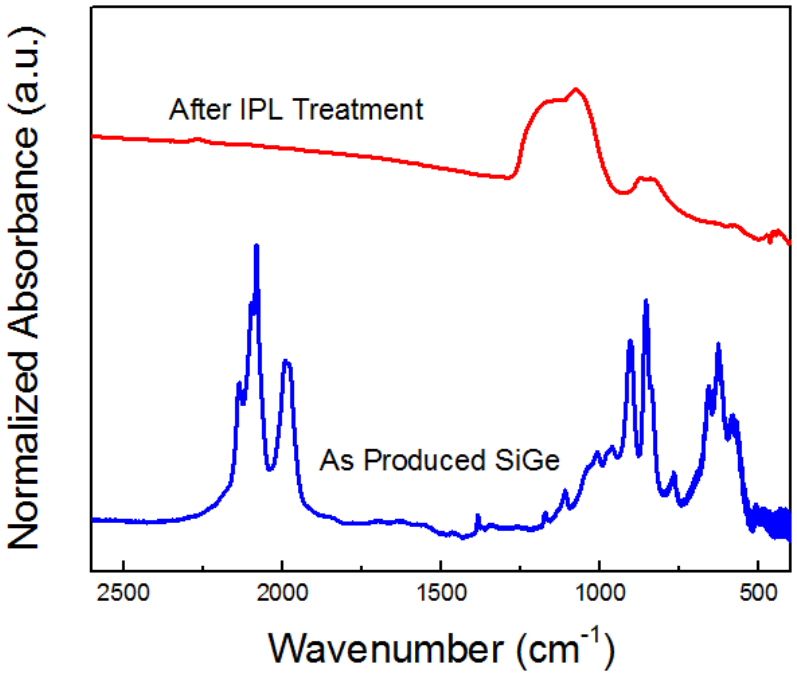

Figure 30: FTIR of IPL-treated SiGe. Little to no hydrogen bonds remain after a single IPL pulse.

Undoped $Si_{0.8}Ge_{0.2}$ was deposited to be about 4 µm thick on fused quartz. It was treated with 1250 one-millisecond IPL pulses. The film in the middle of the sample flaked away, and the sides of the sample turned an opaque brown (Figure 31). SEM was done on the edge of the sample and on the internal flaking portion.

Figure 31: Photo of SiGe film on fused quartz after IPL treatment. IPL parameters: 3 kV, 1 ms, 1250 pulses.

SEM of the sample showed vastly different film morphologies between the edge and middle of the sample. The middle has flaking pieces which, when magnified, have 1-5 µm spheres of germanium in the center of the flake (Figure 32 (a)). The back of the flake is still relatively smooth by comparison. It even appears that small hair-like crystal structures are

growing out of the flake. EDX of the flake shows there is higher germanium content inside the flake where spheres of germanium appear to percolate out. The outside has a higher silicon content. The outer edge of the sample shows a less drastic change, although the sample does experience extensive cracking. These results indicate that the middle of the sample is getting much hotter during IPL treatment than the edge of the sample. XRD on the edge of the sample reveals an average grain size of 37 nm. It was not possible to get good XRD data from the flaking portion of the sample.

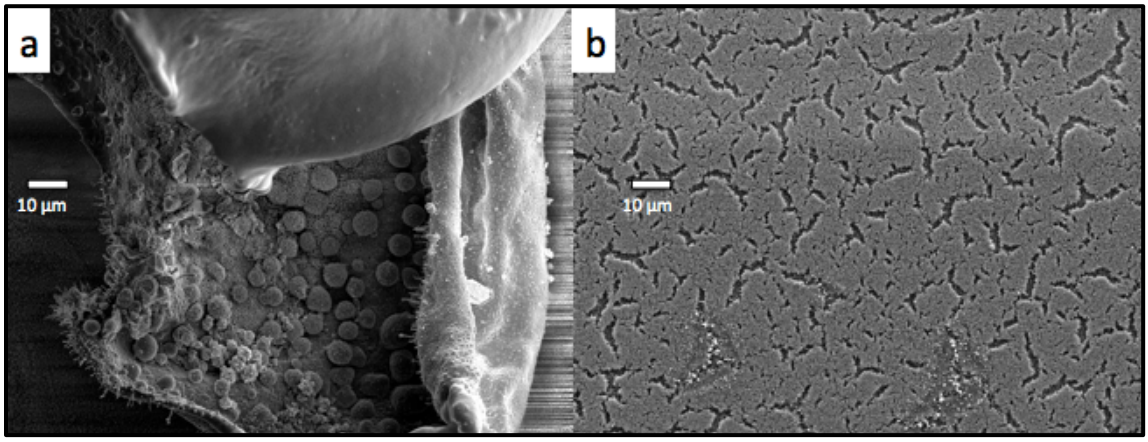

Figure 32: SEM of IPL on fused quartz. Images of an SiGe film on fused quartz after 1250 one-millisecond pulses at 3 kV (a) in the middle of the sample where flaking occurred and (b) in a smoother area on the edge.

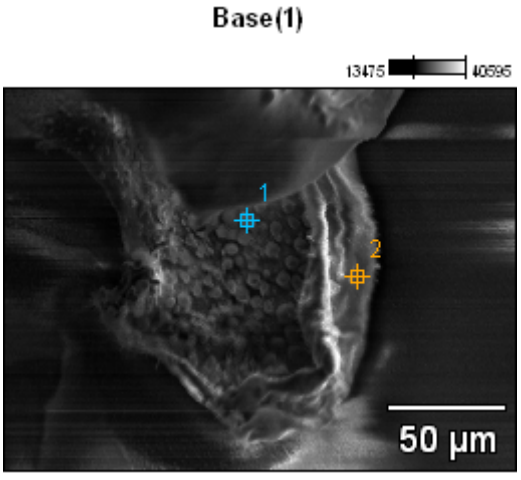

Figure 33: EDX of a flake of IPL-Treated SiGe. The inside shows higher germanium content than the back of the flake.

Point	*Si*	*Ge*
1	54.50 +/- 0.29	45.50 +/- 1.89
2	83.03 +/- 0.45	16.97 +/- 2.79

The same procedure was attempted with one-fifth the number of pulses (250), resulting in the same flaking. XRD of this sample indicated grain growth to 45 nm. This does not necessarily mean that fewer pulses led to an increase in grain growth. The XRD measurement of the 250 pulse sample could have been closer toward the sample center where grain growth was higher. Additionally, XRD does not always provide accurate size information at these larger grain scales. A third sample was IPL treated at 3 kV for a single 1 ms pulse. Cracking and flaking were just beginning in this sample. The power and pulse length used was too aggressive for sintering the film. Further, the fused quartz substrate has a poor thermal conductivity that does not conduct away heat efficiently, leading to excess sample heating.

To address the issue of cracking, films were also deposited on silicon wafer and treated with single pulses of intense light of 1 ms in duration. Samples treated at both 3 kV and 2 kV exhibited a color change that was inconsistent throughout the sample. Figure 34 shows the film before (a) and after IPL (b).

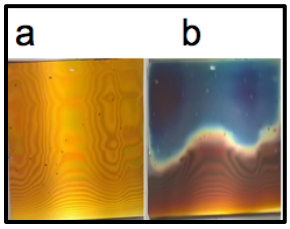

Figure 34: Photo of SiGe film on Si wafer before (a) and after (b) IPL treatment.

XRD was done on both sides of the two-toned film. Average grain size in the blue half had grown to 17 nm while the brown side did not show any grain growth. SEM confirmed that no morphological changes had occurred to the brown side of the film, while the blue side showed spheres on the order of 250 nm had percolated to the surface of the film (Figure 35). Since germanium absorbs more of the spectrum emitted by the xenon lamp than silicon, these spheres were assumed to be germanium rich or solely germanium. EDX again confirmed that the spheres have a much higher content of germanium than the surrounding material.

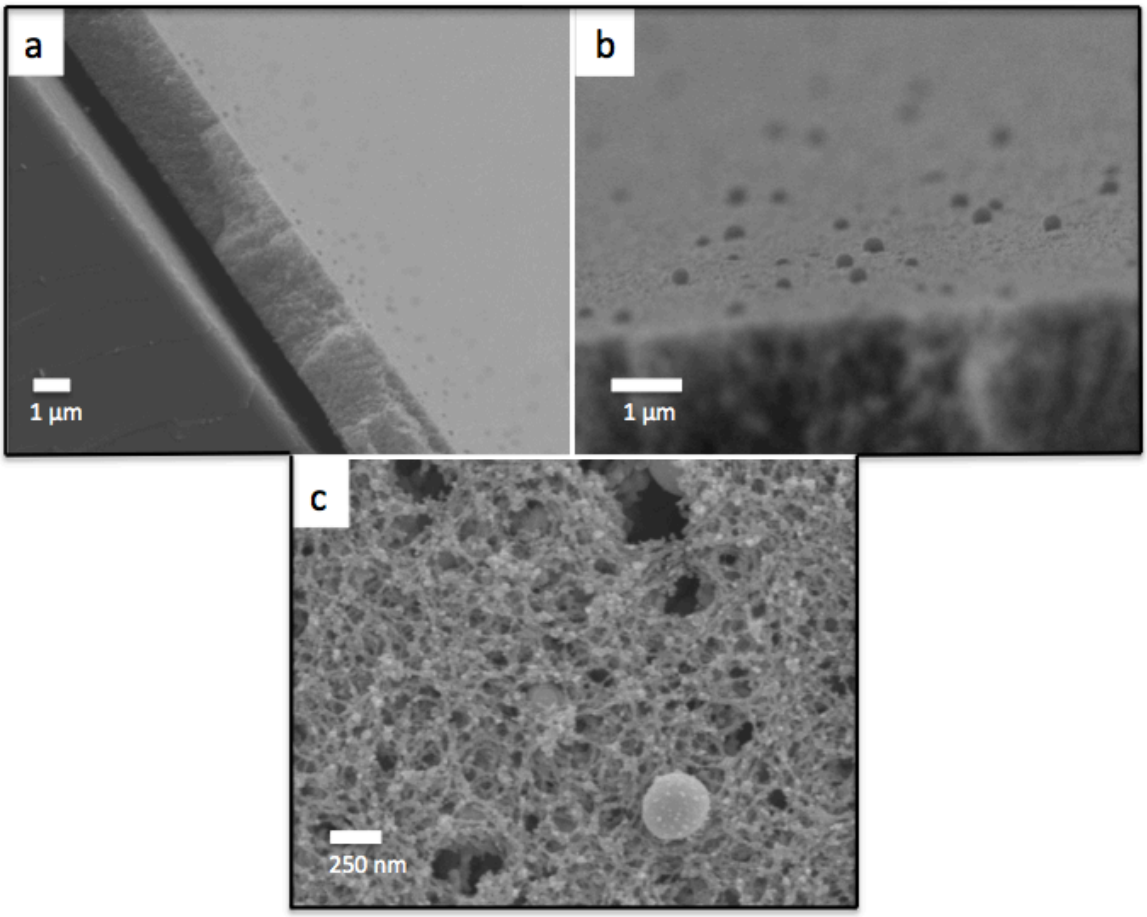

Figure 35: SEM of IPL SiGe on an Si wafer. A single 1 ms pulse at 2 kV caused delamination of the film (a) and percolation of the germanium to the surface - (b) and (c).

The germanium spheres sit on top of a sintered web of SiGe with a lower germanium content than films before IPL sintering (Figure 33 (c)). The web appears to have slightly larger grains than in unsintered reference samples. The web-like structure is not likely to provide good electrical conductivity, and germanium diffusing to the surface of the sample will likely increase thermal conductivity due to the reduction of germanium in the SiGe lattice.

The sample treated at 3 kV showed the same germanium percolation, with a higher density of germanium-rich spheres on the film surface (Figure 35 (a)). Cross-sectional SEM of the film also shows an apparent penetration depth to the sintering (Figure 35 (b)). Large

sintered areas are visible in the top 500 nm of the film. Below that, the sample does not appear sintered.

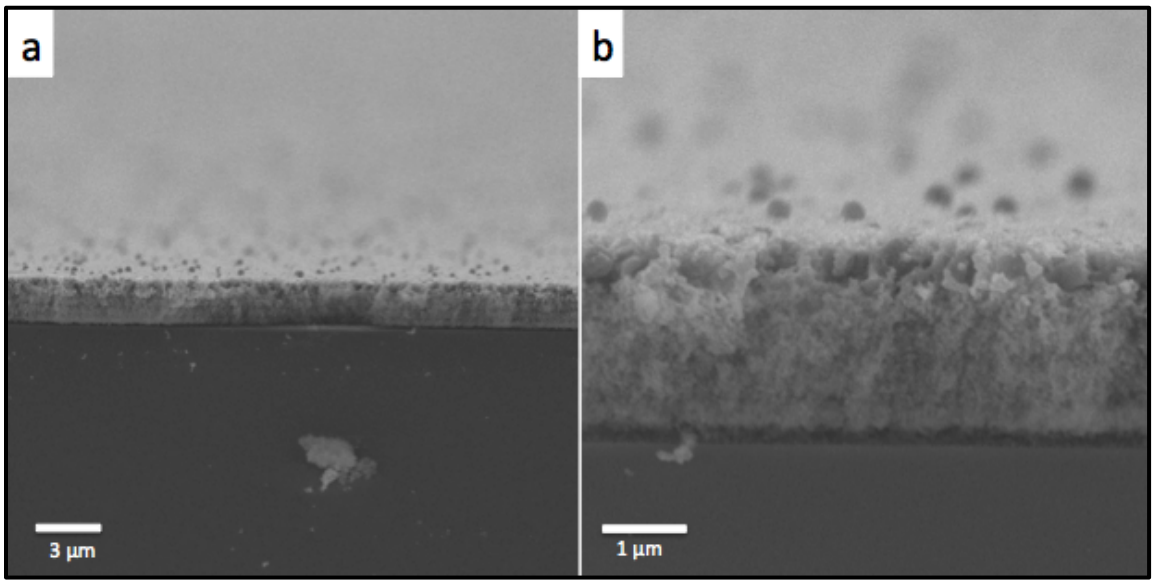

Figure 36: Cross-sectional SEM of IPL sintering depth. A single 1 ms pulse at 3 kV shows a higher density of germanium (a) that has percolated to the surface than in the 2 kV sample in Figure 32. A higher magnification shows a sintering depth of about 500 nm at the top of the sample (b).

The two-toned color of both samples and XRD indicate that half of the samples were not sintered. Variations in film thickness occur as a result of the deposition process. Variations in density are also likely near the edges of the particle stream, as discussed in the ellipsometric results. Samples of two different thicknesses were treated with IPL to determine whether sample thickness affected sintering.

Films were deposited by swiping the nanoparticle stream over an area of 10 cm for 15, 30, 60, and 90 second periods. IPL treatment was done on each sample for a single one-millisecond pulse at 3 kV. SEM was done to obtain cross sectional images (Figure 36) and top down images (Figure 37). Fifteen and thirty-second depositions did not show any morphological difference from the reference sample in cross-sectional images. The sixty-second sample shows a sintering penetration depth of about 400 nm. The ninety-second sample shows sintered grains for over 700 nm.

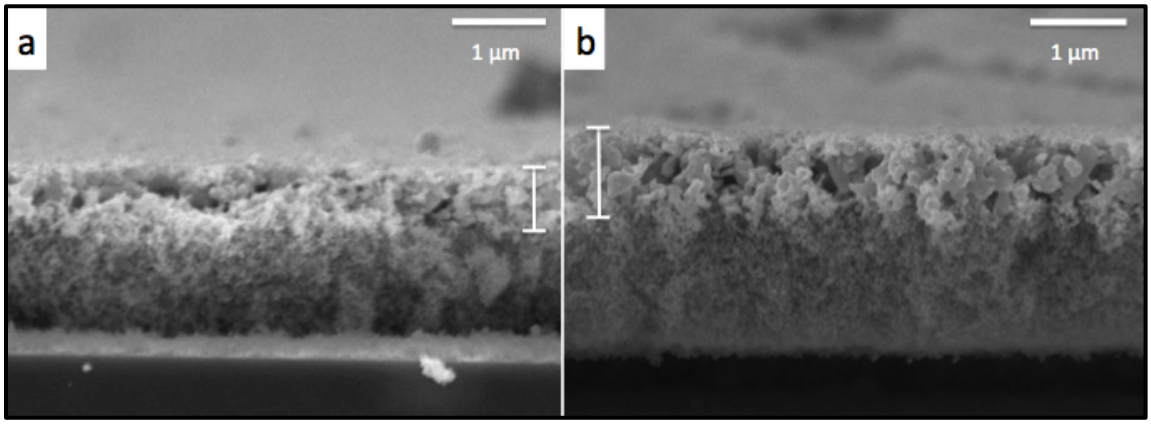

Figure 37: SEM of sintering penetration depth variations. (a) 60-second deposition shows a grain growth depth of under 400 nm while a deposition of 90 seconds shows a grain growth depth of over 700 nm, indicating that the grain growth depth is dependent on thickness of the film rather than the penetration depth of light during IPL treatment. Images by Claudia Gorynski on a JEOL 6700 SEM.

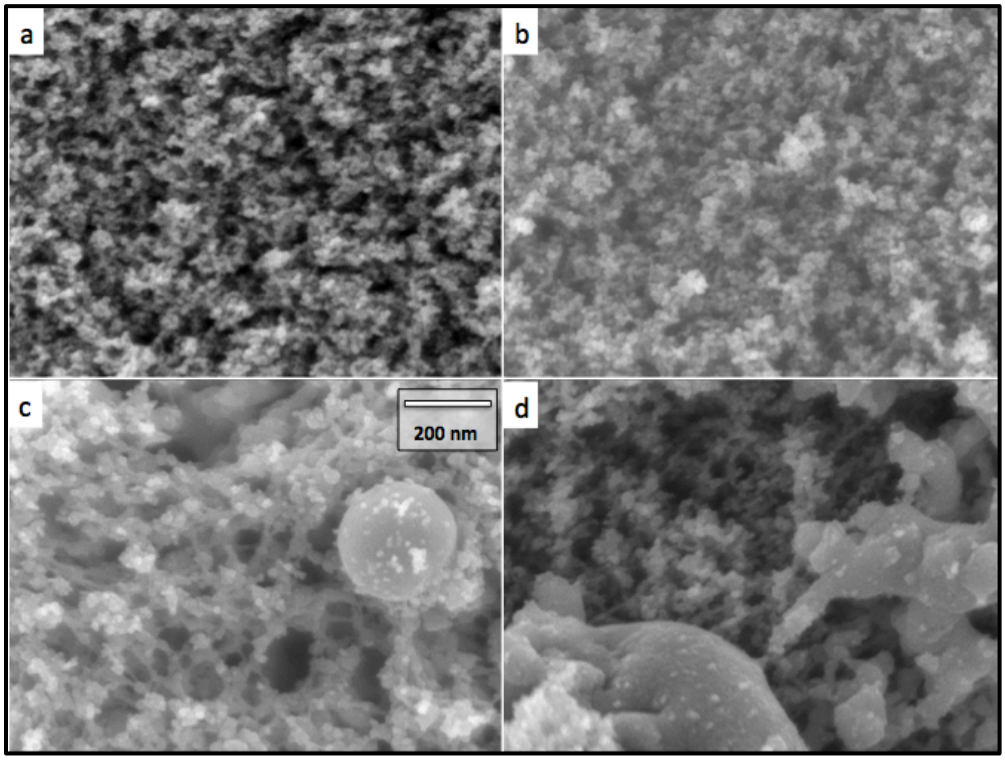

Figure 38: SEM images of IPL-treated SiGe films deposited by inertial-impaction swiping for 15 s (a), 30 s (b), 60 s (c), and 90 s (d) show that aggregate heating effects in thicker samples cause more germanium to percolate out of the film to the surface.

Similarly, top down images of the 15 and 30 second depositions do not visibly display morphological changes. The sixty-second deposition shows germanium percolation to the surface. The ninety-second deposition shows larger blobs of germanium on the surface that have lost spherical shape. Thicker samples have larger sintering penetration depths. Aggregate heating effects with more material to absorb the xenon lamp emissions are more likely to be the cause of the sintering depth than the penetration depth of the light itself.

To investigate density effects, samples were compacted with 4000 lbs of force. One sample was compacted before IPL sintering (Figure 38 (a)) and one after IPL treatment (Figure 38 (b)). The sample compacted before IPL treatment has a few distinguishable morphological features and appears uniform and dense. No grain growth is visible in the SEM after treatment. In the sample compacted after IPL treatment, there are large web-like structures and visible grain growth. Compacting the sample before IPL is therefore preferable. However, in the compaction process, some of the nanoparticle film was lost to the compaction tools. A non-destructive compaction method would have to be determined to obtain reliable films by this method.

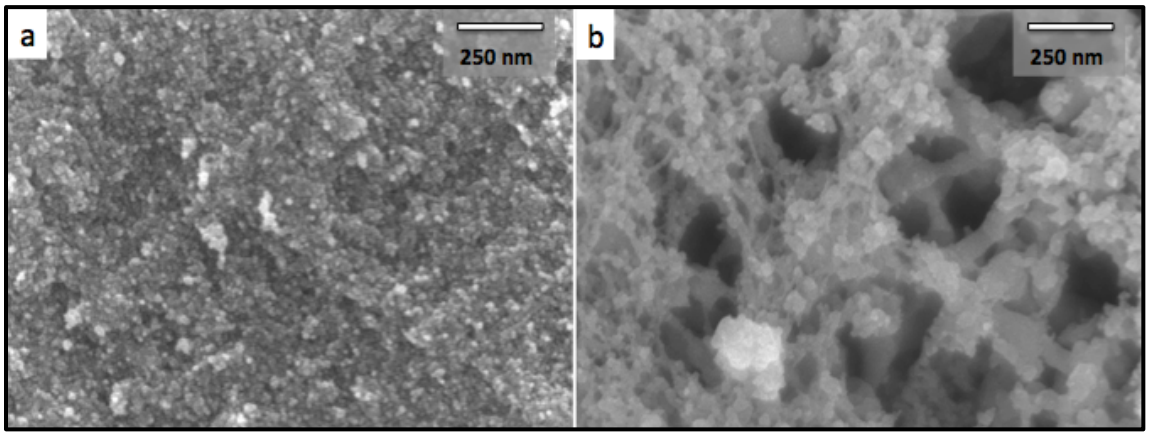

Figure 39: SEM images of an SiGe NC film compacted with 4000lbs of force before IPL treatment (a) and after IPL treatment (b).

Only undoped samples were treated with IPL. The xenon lamp is in air, and the possibility of dopants being released into the laboratory air was deemed too dangerous to

treat doped samples. IPL treatment in air is not ideal since any heating speeds the oxidation reaction and leads to layers of SiO_2 on the surface of the nanoparticles. A method to keep samples under vacuum or in nitrogen during treatment was developed but has not yet been tested.

Glass tubes were fabricated at the University Glass Shop with an inner diameter of 1 cm. One end of the tube was sealed into a half-sphere shape, making the tube look like a long vial. The other end of the tube was placed into an ultra-Torr fitting, which was connected to a kwik flange ISO (KF) vacuum fitting with a ball valve in the middle. The tube can be isolated by closing the ball valve. The KF fitting connects to a vacuum "tree" where several of the tubes can be placed under vacuum. A roughing pump is succeeded by a turbo pump to ensure good vacuum.

The tubes and fittings are loaded with samples and assembled in the nitrogen-purged glovebox. They can be left under nitrogen or pumped down to vacuum. The entire assembly can then be placed under the xenon lamp, IPL treated, and removed back to the glovebox. The electrical properties are expected to be much better without exposure to oxygen during the IPL process. Doped samples can also be treated with no danger to the researcher.

Intense pulsed light treatment needs to be further investigated to assess its full potential in sintering silicon germanium. Problems with unfavorable film morphologies and oxidation were encountered. However, by finding the right lamp parameters and placing the sample in an inert environment, this treatment could be extremely useful in sintering thin films. Roll-to-roll processing or sintering of 3D structures could be made possible. Problems with sample uniformity were seen as a result of film variations, but IPL treatment had uniform results across the surface of the film, in contrast to the Gaussian variation seen in laser treatments.

CHAPTER 4: THERMOELECTRIC PROPERTIES

4.1 ELECTRICAL RESISTIVITY MEASUREMENTS

To assess the effect of IPL treatment on electrical conductivity, resistivity measurements were attempted. Two popular methods were used – the four-point-probe method and the Van der Pauw method. Both measurements were performed on a four-point probe station in the Aydil Photovoltaics Lab at the University of Minnesota.

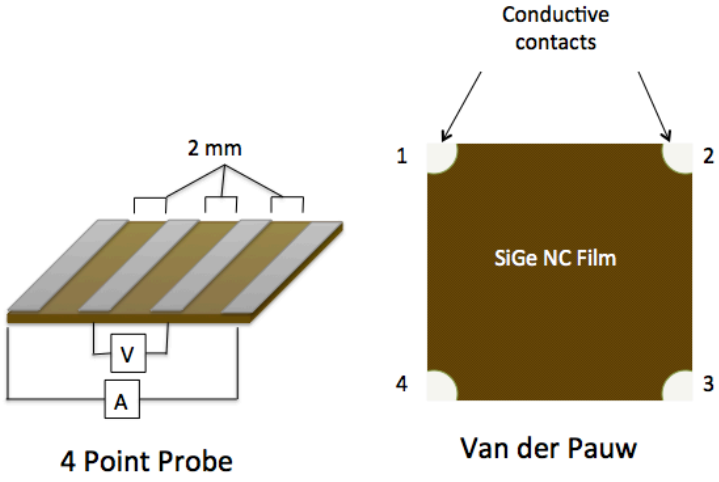

Figure 40: Electrical resistivity measurement contact placement. The four-point probe and Van Der Pauw methods were employed to measure resistivity.

Films were deposited on an undoped silicon wafer with a 300 nm thermal oxide as an insulating substrate. The substrates were cut to 5 mm by 10 mm for the four-point probe measurements and 7 mm by 7 mm for the Van der Pauw method. Two samples were deposited on 1 cm by 1 cm fused quartz. IPL parameters described in section 3.6 were used to treat the samples. 300 nm aluminum contacts were evaporated onto the rectangular four-point substrates and the corners of the square fused quartz substrates as shown in Figure 40 using a steel mask to provide accurate spacing. No mask was available to accommodate the 7 mm by 7 mm samples. Silver paint was applied to the corners of the sample by hand.

The four-point probe measurements were taken by applying a current to the outer two contacts and measuring the voltage between the inner two contacts. This eliminates the effect of contact resistance in the measurement. Several currents are applied and measured against voltage. The data is plotted and fit to a line. The slope of this line represents the resistance provided by Ohm's Law. The resistance can be used to find electrical resistivity by knowing the dimensions of the sample. For the four-point method with 2 mm spacing in between contacts on a sample of 5 mm width, resistivity, ρ, can be found through the equation,

$$\rho = \frac{1}{\sigma} = \frac{R * thickness * 5\ mm}{2\ mm}$$

where the thickness can be determined by doing cross-sectional SEM on the sample.[66]

For the Van der Pauw method, a current is applied to two adjacent contacts while the voltage is measured from the other two. This procedure is repeated with two different contacts (rotating around the sample) and the data analyzed to get a sheet resistivity, R_s, from the equation,

$$1 \approx e^{\frac{-\pi * R_{12,34}}{R_S}} + e^{\frac{-\pi * R_{23,41}}{R_S}}$$

where the subscripts of R express which two electrodes had a current applied, followed by which two had voltage measured. The resistivity is then determined from the equation,

$$\rho = \frac{1}{\sigma} = R_s * thickness$$

where the area of the sample cancels as it is a square.

Fifteen samples were tested for resistivity using these methods. Unfortunately, in the 7 mm by 7 mm substrates, the silver paint did not appear to make an Ohmic contact with the sample. There may also have been effects from the silver paint touching the substrate edges where no thermal oxide was present. The samples with aluminum contacts only showed noise on the order of femtovolts. Currents were applied from 0 to 1, 0 to 10, and 0 to 100 nA

with voltage sweeps from -1 to 1 and -10 to 10 V. No measurements could be obtained. The undoped sample is likely too resistive to measure, even after IPL treatment. Doped samples would provide better measurements.

4.2 SEEBECK COEFFICIENT MEASUREMENTS

A device for measuring the Seebeck coefficient of a material is available in the Department of Physics in the lab of Professor Kakalios. This device has two heated posts 4 mm apart. The sample is placed on top the posts so that a temperature gradient is established across the sample. Aluminum contacts are evaporated onto the sample for electrical contacts with a 4 mm separation distance. Silver paint attaches a small electrical probe to the aluminum contacts on each side of the sample. On the other end of the sample, electrically isolated from the electrical probes, two thermocouples measure the temperature difference across the sample (Figure 41). A Lab View program controls the temperature of the posts separately between room temperature and 450°K. It records the temperature difference and voltage and plots them against each other to obtain the Seebeck coefficient.

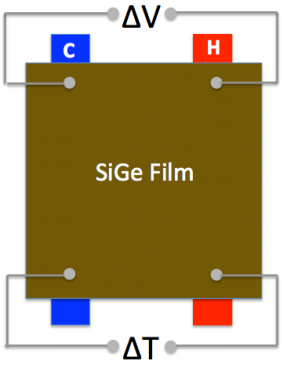

Figure 41: Schematic for Seebeck coefficient measurements.

The high resistivity of the undoped samples will make it difficult to get an accurate measurement of the Seebeck coefficient. Once doped samples can be treated, this tool will be extremely valuable in making measurements to determine thermoelectric figure of merit.

4.3 THERMAL CONDUCTIVITY MEASUREMENTS

Thermal conductivity of a nanostructured SiGe sample is almost guaranteed to be low. To determine a quantitative value, measurements can be done using a time-domain thermoreflectance (TDTR) technique by Professor Wang's Mechanical Engineering group at the University of Minnesota. TDTR is a laser technique where a microscopic objective lens focuses pump and probe beams. The pump beam pulses, and heat spreads around the pulse center. A probe beam is located near the pump beam. The probe beam measures changes in reflectivity, a temperature-dependent property.[67] From this, a heat transfer model determines the thermal conductivity of the material.

Since thermal conductivity reduction is the primary means of ZT increase in nanostructured thermoelectric materials, the TDTR measurement is an important one. First, a post-synthesis sample treatment technique must produce a sample of sufficient electrical conductivity to provide a reasonable ZT. Once good electrical conductivity is established, thermal conductivity measurements can provide the final step in determining the thermoelectric efficiency of the material.

CHAPTER 5: CONCLUSIONS

5.1 RESEARCH SUMMARY

Several avenues of sintering silicon germanium have been explored. Thermal annealing remains a reliable method, but the high temperatures required severely limit substrate choices. Hot pressing has been successful for other research groups, however, in this work, high enough pressures were not achieved to get a fully dense sample. Further, multiple phases were seen in the resulting samples and undesirable grain growth occurred.

Intense pulsed light sintering remains an intriguing area of research. Since only undoped samples could be treated safely, it is difficult to tell how much the electrical conductivity was improved during the process. However, structural changes show that the film is responding well to the light. Given that the xenon lamp was not designed for this specific application, it is clear that lamps with slightly different wavelengths or intensities could be used or designed for processing silicon germanium films. If sintering can be achieved in a few or even a single pulse, this would have immense implications for processing films quickly, in unique structures, or on novel substrates. Given the potential applications, several ideas and suggestions for future research are presented.

5.2 SUGGESTIONS FOR FUTURE RESEARCH

IPL treatment of phosphorous and boron doped samples will provide significantly better opportunity for characterization. The vacuum or inert gas environment of the tube design described in section 3.6 will make this possible. Electrical resistivity and Seebeck coefficient measurements will provide valuable feedback on the quality of the sintering occurring. Once a high electrical conductivity sample is obtained, thermal conductivity measurements will round out the figure of merit measurements.

Experiments have shown that substrate choice is important to the sintering process. Finding the ideal substrate for IPL treatment and exploring flexible substrates will be of interest. Compacting the samples without losing portions of the film will lead to better

electrical conductivity through increased nanoparticle contact. Modulation doping, where doped NCs are embedded in an undoped matrix, could lead to electrical improvements. By providing an undoped matrix, charge carriers emerging from the doped NCs can move freely through the matrix without encountering point defect scattering caused by dopant incorporation in the lattice of doped particles.[68,69]

Creating an ellipsometry model that accurately measures the density of SiGe with a small SiO_2 layer would make characterization of the thin films faster. Many resources exist in the literature for SiGe optical constants[70] and determining composition of SiGe.[71–74] Our model would have to accommodate dopants, inconsistent grain sizes, and varying densities. Other researchers have been able to make spectroscopic ellipsometry measurements of density with 90% certainty.[75] Such a model would show density changes from post-synthesis treatments, IPL or otherwise, in uncompacted samples.

There are many more possibilities to improve the thermoelectric properties of silicon germanium. Incremental improvements lead to great improvement over time. Perhaps at some future time, a new set of Voyager probes will leave the solar system sporting the research discoveries of today.

REFERENCES

1. DeWinter, F., Stapfer, G. & Medina, E. The Design of a Nuclear Power Supply with a 50 Year Life Expectancy: The JPL Voyager's SiGe MHW RTG. *IEEE Aerosp. Electron. Syst. Mag.* **15,** 5–12 (2000).

2. Haxel, G. B. *et al.* Rare Earth Elements — Critical Resources for High Technology. *United States Geol. Surv. Fact Sheet* **087,** 4 (2002).

3. Rowe, D. M. *CRC Handbook of Thermoelectrics*. (CRC Press, 1995).

4. Cressler, J. & Niu, G. *Silicon-Germanium Heterojunction Bipolar Transistors*. (Artech House, 2003).

5. Kasper, E. & Lyutovich, K. *Properties of Silicon Germanium and SiGe-Carbon*. (Institution of Electrical Engineers, 2006).

6. Kraemer, D., McEnaney, K., Chiesa, M. & Chen, G. Modeling and optimization of solar thermoelectric generators for terrestrial applications. *Sol. Energy* **86,** 1338–1350 (2012).

7. Strasser, M., Aigner, R., Franosch, M. & Wachutka, G. Miniaturized thermoelectric generators based on poly-Si and poly-SiGe surface micromachining. *Sensors Actuators, A Phys.* **97-98,** 535–542 (2002).

8. Goldsmid, H. J. *Thermoelectric Refrigeration*. (Springer Science+Business Media, 1964).

9. Shakouri, A. & Bowers, J. E. Heterostructure integrated thermionic coolers. *Appl. Phys. Lett.* **71,** 1234–1236 (1997).

10. Minnich, A. J., Dresselhaus, M. S., Ren, Z. F. & Chen, G. Bulk nanostructured thermoelectric materials: current research and future prospects. *Energy Env. Sci* **2,** 466–479 (2009).

11. Koumoto, K. & Mori, T. *Thermoelectric Nanomaterials*. **182,** (2013).

12. Slack, G. A. & Hussain, M. A. The maximum possible conversion efficiency of silicon-germanium thermoelectric generators. *J. Appl. Phys.* **70,** 2694–2718 (1991).

13. Zheng, J.-C. Recent advances on thermoelectric materials. *Front. Phys. China* **3,** 269–279 (2008).

14. Snyder, G. J. & Toberer, E. S. Complex thermoelectric materials. *Nat. Mater.* **7,** 105–114 (2008).

15. Liu, W., Yan, X., Chen, G. & Ren, Z. Recent advances in thermoelectric nanocomposites. *Nano Energy* **1,** 42–56 (2012).

16. Levinshtein, M. E., Rumyantsev, S. L. & Shur, M. S. *Properties of Advanced Semiconductor Materials GaN, AlN, SiC, BN, SiC, SiGe*. (2001).

17. Dismukes, J. P., Ekstrom, L., Steigmeier, E. F., Kudman, I. & Beers, D. S. Thermal and electrical properties of heavily doped Ge-Si alloys up to 1300K. *J. Appl. Phys.* **35,** 2899–2907 (1964).

18. Vining, C. B. A model for the high-temperature transport properties of heavily doped n-type silicon-germanium alloys. *J. Appl. Phys.* **69,** 331–341 (1991).

19. Hicks, L. D. & Dresselhaus, M. S. Thermoelectric figure of merit of a one-dimensional conductor. *Phys. Rev. B* **47,** 16631–16634 (1993).

20. Wang, X. W. *et al.* Enhanced thermoelectric figure of merit in nanostructured n-type silicon germanium bulk alloy. *Appl. Phys. Lett.* **93,** 1–4 (2008).

21. Joshi, G. *et al.* Enhanced thermoelectric figure of merit in nanostructured p-type silicon germanium bulk alloys. *Nano Lett.* **8,** 4670–4674 (2008).

22. Minnich, A. J. *et al.* Modeling study of thermoelectric SiGe nanocomposites. *Phys. Rev. B - Condens. Matter Mater. Phys.* **80,** 1–14 (2009).

23. Bux, S. K. *et al.* Nanostructured bulk silicon as an effective thermoelectric material. *Adv. Funct. Mater.* **19,** 2445–2452 (2009).

24. Chen, G. *et al.* Increased Phonon Scattering by Nanograins and Point Defects in Nanostructured Silicon with a Low Concentration of Germanium. *Phys. Rev. Lett.* **102,** 2–5 (2009).

25. Vining, C. B., Laskow, W., Hanson, J. O., Van Der Beck, R. R. & Gorsuch, P. D. Thermoelectric properties of pressure-sintered Si0.8Ge 0.2 thermoelectric alloys. *J. Appl. Phys.* **69,** 4333–4340 (1991).

26. Mangolini, L., Thimsen, E. & Kortshagen, U. High-Yield Plasma Synthesis of Luminescent Silicon Nanocrystals. *Nano* (2005).

27. Kortshagen, U. Nonthermal plasma synthesis of semiconductor nanocrystals. *J. Phys. D. Appl. Phys.* **42,** 113001 (2009).

28. Pi, X. D. & Kortshagen, U. Nonthermal plasma synthesized freestanding silicon-germanium alloy nanocrystals. *Nanotechnology* **20,** 295602 (2009).

29. Rowe, D. J. & Kortshagen, U. R. Boron- and phosphorus-doped silicon germanium alloy nanocrystals - Nonthermal plasma synthesis and gas-phase thin film deposition. *APL Mater.* **2,** 2–7 (2014).

30. Lieberman, M. A. & Lichtenberg, A. J. *Principles of plasma discharges and Materials processing*. *Wiler-Interscience* (John Wiley & Sons, Inc, 1994). doi:10.1017/CBO9781107415324.004

31. Holman, Z. C. & Kortshagen, U. R. A flexible method for depositing dense nanocrystal thin films: impaction of germanium nanocrystals. *Nanotechnology* **21,** 335302 (2010).

32. Sidebottom, D. *Fundamentals of Condensed Matter and Crystalline Physics*. (Cambridge University Press, 2012).

33. Kittel, C. *Introduction to Solid State Physics*. (John Wiley & Sons, Inc, 1953). doi:10.1119/1.1933590

34. Dismukes, J. P., Ekstrom, L. & Paff, R. J. Lattice Parameter and Density in Germanium-Silicon Alloys. *J. Phys. Chem.* **437,** 3021–3027 (1964).

35. Langford, J. I. & Wilson, A. J. C. Scherrer after sixty years: A survey and some new results in the determination of crystallite size. *J. Appl. Crystallogr.* **11,** 102–113 (1978).

36. Alonso, M. I. & Winer, K. Raman spectra of c-Si1-xGex alloys. *Phys. Rev. B* **39,** 10056–10062 (1989).

37. Larkin, P. *Infrared and Raman Spectroscopy*. (Elsevier, 2011).

38. Schrotter, J. C., Cardenas, A., Smaihi, M. & Hovnanian, N. Silicon and phosphorus alkoxide mixture: Sol-gel study by spectroscopic technics. *J. Sol-Gel Sci. Technol.* **4,** 195–204 (1995).

39. Saß, M., Annen, A. & Jacob, W. Hydrogen bonding in plasma-deposited amorphous hydrogenated boron films. *J. Appl. Phys.* **82,** 1905 (1997).

40. Shen, S. & Cardona, M. Infrared and Far Infrared Absorption of B- and P-Doped Amorphous Si. *J. Phys. Colloq.* **42,** 349–351 (1981).

41. Annen, A., Beckmann, R. & Jacob, W. Deposition and characterization of dense and stable amorphous hydrogenated boron films at low substrate temperatures. *J. Non. Cryst. Solids* **209,** 240–246 (1997).

42. Kortshagen, U. Nonthermal Plasma Synthesis of Nanocrystals: Fundamentals, Applications, and Future Research Needs. *Plasma Chem. Plasma Process.* **36,** 73–84 (2016).

43. Rowe, D. M., Shukla, V. S. & Savvides, N. Phonon scattering at grain boundaries in heavily doped fine-grained silicon–germanium alloys. *Nature* **290,** 765–766 (1981).

44. Rowe, D. M., Fu, L. W. & Williams, S. G. K. Comments on the thermoelectric

properties of pressure-sintered Si 0.8Ge0.2 thermoelectric alloys. *J. Appl. Phys.* **73,** 4683–4685 (1993).

45. Hausner, H.H., Roll, K.H. and Johnson, P. K. *Perspective in Powder Metallurgy*. *Springer Science+Business Media* **1,** (1967).

46. Bunce, R. W. & Rowe, D. M. The vacuum hot-pressing of germanium and silicon-germanium alloys. *J. Phys. D. Appl. Phys.* **10,** 941 (1977).

47. Takashiri, M., Borca-Tasciuc, T., Jacquot, A., Miyazaki, K. & Chen, G. Structure and thermoelectric properties of boron doped nanocrystalline Si 0.8Ge 0.2 thin film. *J. Appl. Phys.* **100,** 0–5 (2006).

48. Rem, J. B., Holleman, J. & Verweij, J. F. Furnace and rapid thermal crystallization of amorphous GexSil _x and Si for thin film transistors. *Thin Solid Films* **296,** 152–156 (1997).

49. Choi, W. K. *et al.* Germanium diffusion and nanocrystal formation in silicon oxide on silicon substrate under rapid thermal annealing. *Appl. Phys. Lett.* **86,** 86–88 (2005).

50. Peter, C. R., de Souza, J. P. & Hasenack, C. M. Prolonged and rapid thermal annealing of boron implanted silicon. *J. Appl. Phys.* **64,** 2696 (1988).

51. Leveque, P., Mathiot, D., Christensen, J. S., Svensson, B. G. & Larsen, A. N. Effect of a mid-temperature thermal annealing on the enhancement of boron diffusion during rapid thermal annealing. *J. Appl. Phys.* **99,** (2006).

52. Lie, D. Y. C., Song, J. H., Nicolet, M. A. & Theodore, N. D. Advantage of rapid thermal annealing over furnace annealing for P implanted metastable Si / Ge0 . 12Si0 . 88. *Appl. Phys. Lett.* **5,** 592–594 (1995).

53. Steve Jurichich, Tsu-Jae King, Krishna Saraswat, and J. M. Low Thermal Budget Polycrystalline Silicon-Germanium Thin-Film Transistors Fabricated by Rapid Thermal Annealing. *Jpn J. Appl. Phys.* **33,** 1139–1141 (1994).

54. Rowe, D. J. Impurities in Silicon Nanocrystals: The intentional and the inherent, Thesis (Ph.D). (University of Minnesota, 2013).

55. Kleczewski, A. C. Silicon Nanocomposite Development for High Efficiency Thermoelectric Materials Research, Thesis (Master of Science). (University of Minnesota, 2010).

56. Singh, H and Gupta, S. R. Preparation of Germanium-Silicon Thermo-Electric Elements by Hot Pressing. *Phys. Status Solidi Appl. Mater. Sci.* **267,** 267–270 (1971).

57. Bathula, S. *et al.* Enhanced thermoelectric figure-of-merit in spark plasma sintered nanostructured n-type SiGe alloys. *Appl. Phys. Lett.* **101,** (2012).

58. Baldridge, T. Laser sintering of Si-Ge nanoparticles for thermoelectric materials, Thesis (Ph.D). (University of Virginia, 2012).

59. Kang, H., Sowade, E. & Baumann, R. R. Direct intense pulsed light sintering of inkjet-printed copper oxide layers within six milliseconds. *ACS Appl. Mater. Interfaces* **6,** 1682–1687 (2014).

60. Kim, D. W. *et al.* Rapid curing of solution-processed zinc oxide films by pulse-light annealing for thin-film transistor applications. *Electron. Mater. Lett.* **11,** 82–87 (2015).

61. Kang, J. S., Ryu, J., Kim, H. S. & Hahn, H. T. Sintering of Inkjet-Printed Silver Nanoparticles at Room Temperature Using Intense Pulsed Light. *J. Electron. Mater.* **40,** 2268–2277 (2011).

62. Kim, H. S., Dhage, S. R., Shim, D. E. & Hahn, H. T. Intense pulsed light sintering of copper nanoink for printed electronics. *Appl. Phys. A Mater. Sci. Process.* **97,** 791–798 (2009).

63. Ryu, J., Kim, H.-S. & Hahn, H. T. Reactive Sintering of Copper Nanoparticles Using Intense Pulsed Light for Printed Electronics. *J. Electron. Mater.* **40,** 42–50 (2011).

64. Della Gaspera, E. *et al.* Flash-assisted processing of highly conductive zinc oxide electrodes from water. *Adv. Funct. Mater.* **25,** 7263–7271 (2015).

65. Drahi, E., Blayac, S., Borbely, A. & Benaben, P. Impact of ink synthesis on processing of inkjet-printed silicon nanoparticle thin films: A comparison of Rapid Thermal Annealing and photonic sintering. *Thin Solid Films* **574,** 169–176 (2015).

66. Singh, Y. Electrical Resistivity Measurements: a Review. *Int. J. Mod. Phys. Conf. Ser.* **22,** 745–756 (2013).

67. Zhu, J. *et al.* Ultrafast thermoreflectance techniques for measuring thermal conductivity and interface thermal conductance of thin films. *J. Appl. Phys.* **108,** (2010).

68. Yu, B. *et al.* Enhancement of thermoelectric properties by modulation-doping in silicon germanium alloy nanocomposites. *Nano Lett.* **12,** 2077–2082 (2012).

69. Zebarjadi, M. *et al.* Power factor enhancement by modulation doping in bulk nanocomposites. *Nano Lett.* **11,** 2225–2230 (2011).

70. G.E.Jellison Jr, T. E. H. Optical functions of silicon — germanium alloys determined using spectroscopic ellipsometry. *Opt. Mater. (Amst).* **2,** 105–117 (1993).

71. Ferrieu, F., Ribot, P. & Regolini, J. L. Spectroscopic ellipsometry of Si x Ge 1-x / Si : a tool for composition and profile analysis in strained heterostructure used in the microelectronics industry . 96–99 (1999).

72. Ferrieu, F., Morin, C. & Regolini, J. L. Optical characterization by spectroscopic ellipsometry of polycrystalline Si 1 y x Ge x of variable Ge composition up to 100 % Ge. 316–321 (1998).

73. Broschwitz, M., Dettmer, K. & Schoenes, J. Independent determination of Ge content in thin Si[sub 1−x]Ge[sub x] quantum wells by spectroscopic ellipsometry. *Appl. Phys. Lett.* **77,** 367 (2000).

74. Racanelli, M. *et al.* Ellipsometry for rapid characterization of Si1-xGex layers. *Appl. Phys. Lett.* **60,** 2225–2227 (1992).

75. Yu, G. *et al.* Characterization of excimer laser annealed polycrystalline Si[sub 1−x]Ge[sub x] alloy thin films by x-ray diffraction and spectroscopic ellipsometry. *J. Appl. Phys.* **83,** 174 (1998).